Détection de rayonnement à très

basses Température

4ème Ecole d'Automne D'Aussois : Balaruc les Bains 14- 20 Novembre 1999

Superconducting Tunnel Junctions

As photon detectors

Roland den Hartog

Superconducting Tunnel Junctions as photon detectors

A practical introduction

Roland den Hartog

Astrophysics Division, ESA – ESTEC

Noordwijk, The Netherlands

Our goal: *Development of high-resolution photon-counting imaging spectrometers for NIR to X-ray based on STJs.*

Our motto: *In theory, practice and theory are equal; in practice, they differ.*

Contents

- Superconductors vs. semiconductors
- STJs: lay-out
- Quasi-particles
- I-V characteristics as a diagnostic tool
- Relevant quasi-particle and phonon processes
- STJ spectroscopy and energy resolution
- New developments at ESTEC

Superconductors versus Semiconductors

- *Charge output:* $Q = E / \varepsilon$
- *Energy resolution:* $\frac{\Delta E}{E} = \sqrt{\frac{F\varepsilon}{E}}$

		Super	*Semi*
Energy / bandgap	Δ_{gap}	0.4 – 1.6 meV	0.7 – 2.7 eV
Single charge creation energy	ε	1.75 Δ_{gap}	1 – 2 Δ_{gap}
Fano factor	F	0.2	0.15
Energy resolution (FWHM, @ 6 keV)	$\Delta E/E$	~ 0.03 %	~ 1 %
Operating temperature	T	0.3 – 1.2 K	170 – 260 K
Pulse-decay time	τ	1 – 20 μs	few μs

A typical STJ in theory...

typical dimensions:

- size: 10 – 200 μm
- base electrode: 100 nm
- Al / AlOx: 5 – 100 nm
- top electrode: 50 – 200 nm

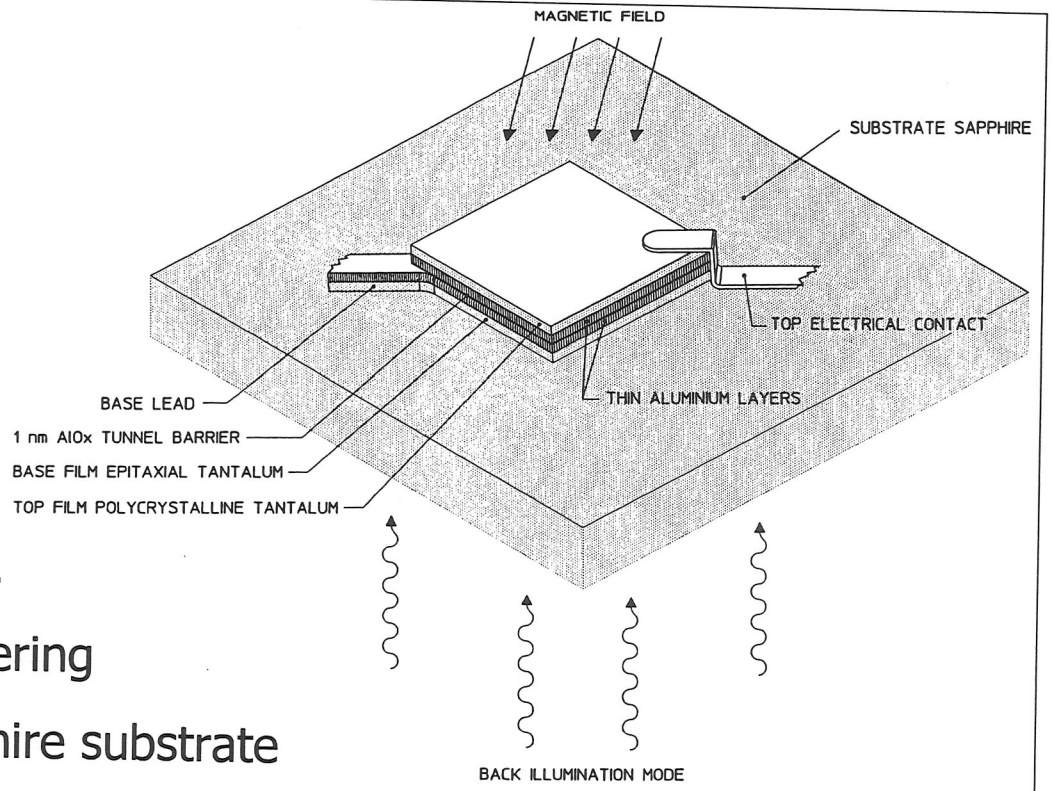

materials: Nb/Al, Ta/Al, V/Al...

- deposition by magnetron sputtering
- base film is epitaxial with sapphire substrate
- top film is poly-crystalline

… and in practice:

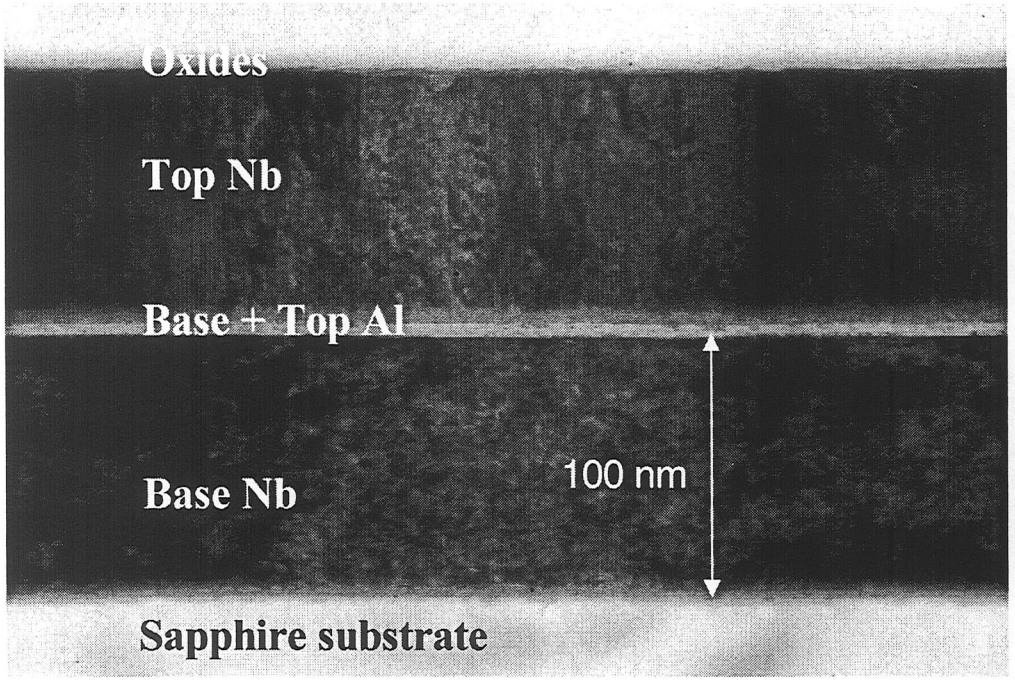

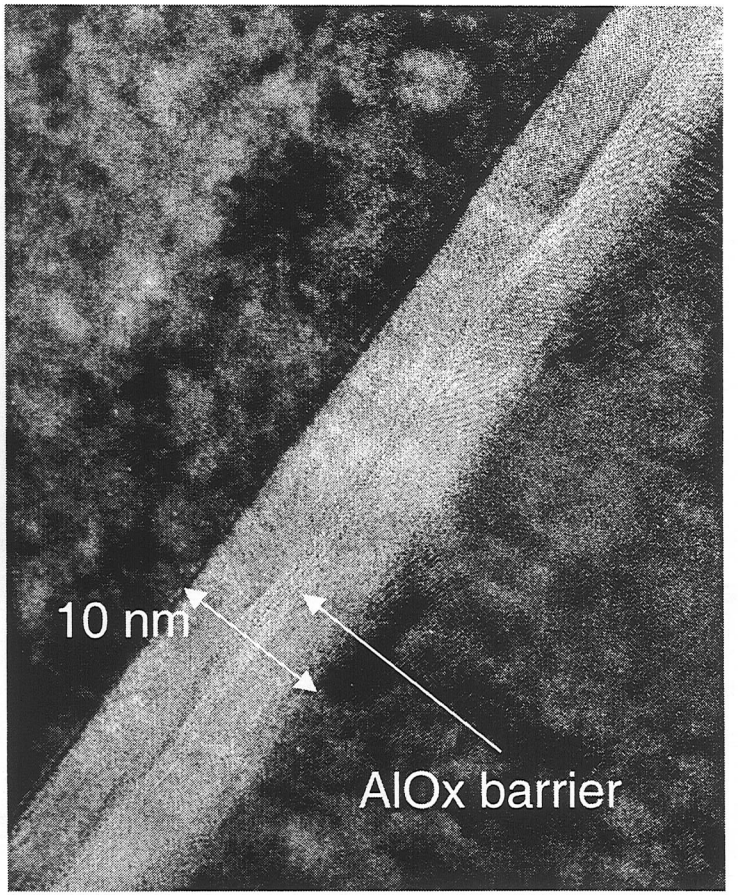

TEM cross-sections of Nb/Al STJs

What is a quasi-particle?

QPs are (superpositions of) excitations of the superconducting groundstate, which is formed by the sea of Cooper pairs.

- QPs can be either electron-like or hole-like
- QPs which have an energy exactly equal to the gap Δ, are 50% electron- and 50% hole-like and have zero velocity.
- In the limit of large energies, QP states become electronic

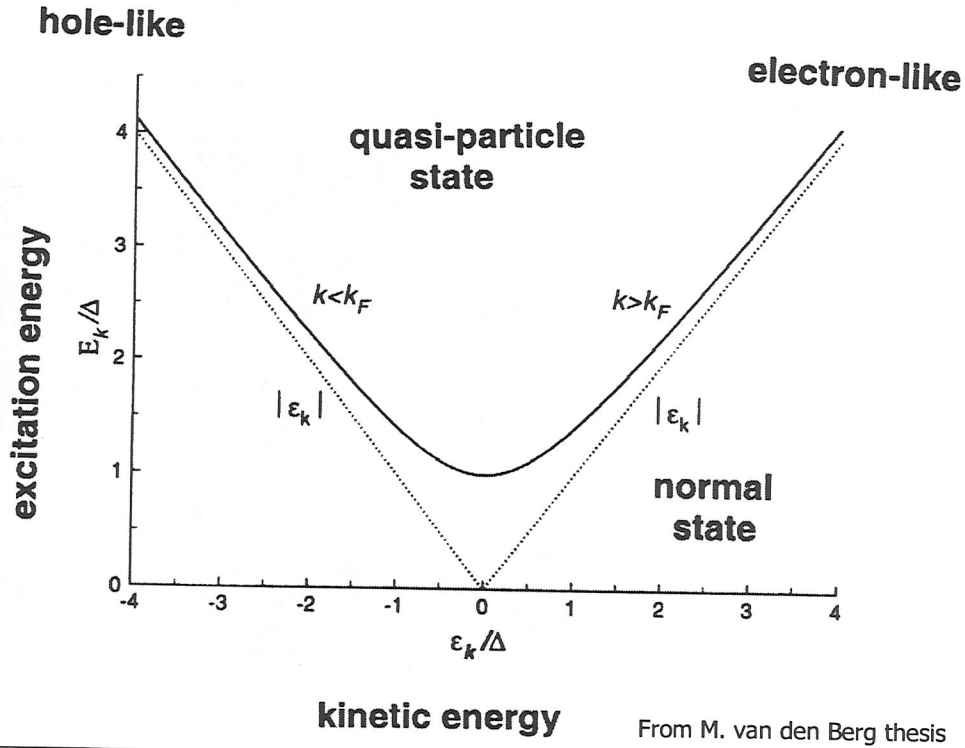

From M. van den Berg thesis

Quasi-particle tunneling in theory...

$$I_{\text{tun}} = I^{(1)}_{1\to 2,e} + I^{(2)}_{2\to 1,h} - I^{(-1)}_{2\to 1,e} - I^{(-2)}_{1\to 2,h}$$

$$I^{(1)}_{1\to 2,e} = \frac{1}{eR_N}\int_{\Delta_1}^{\infty} dE\, N_1(E) N_2(E+eV_b) f(E)\left[1 - f(E+eV_b)\right]$$

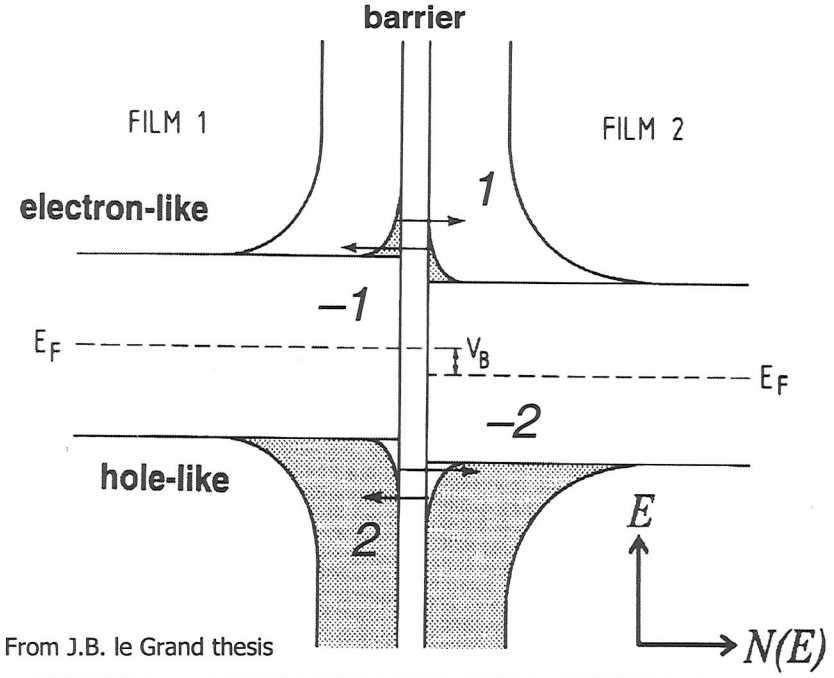

From J.B. le Grand thesis

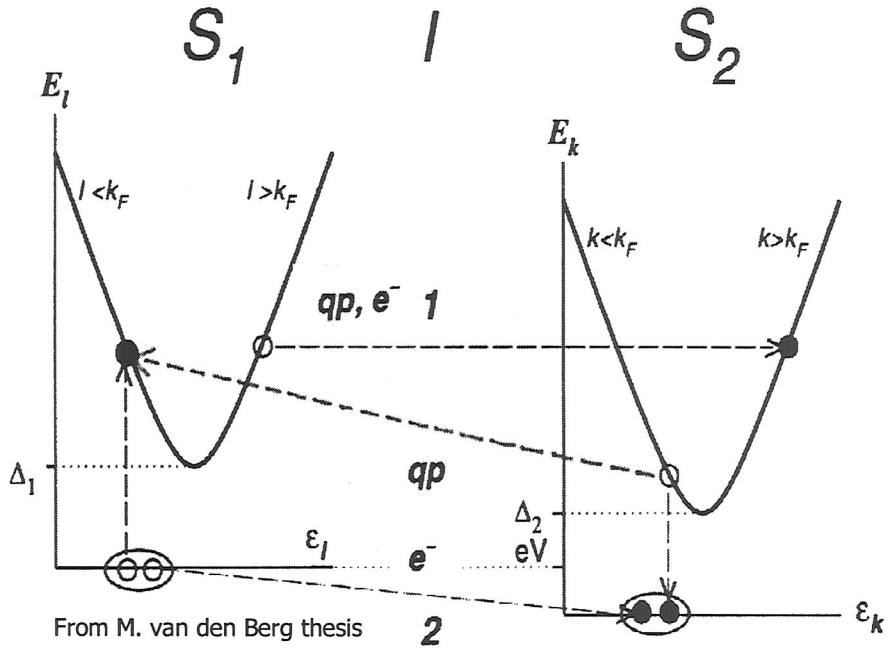

From M. van den Berg thesis

... and practice

- $Q_{out} = \int I_{tun}\, dt$
- Difference between theoretical and measured response probably due to bias fluctuations during pulse

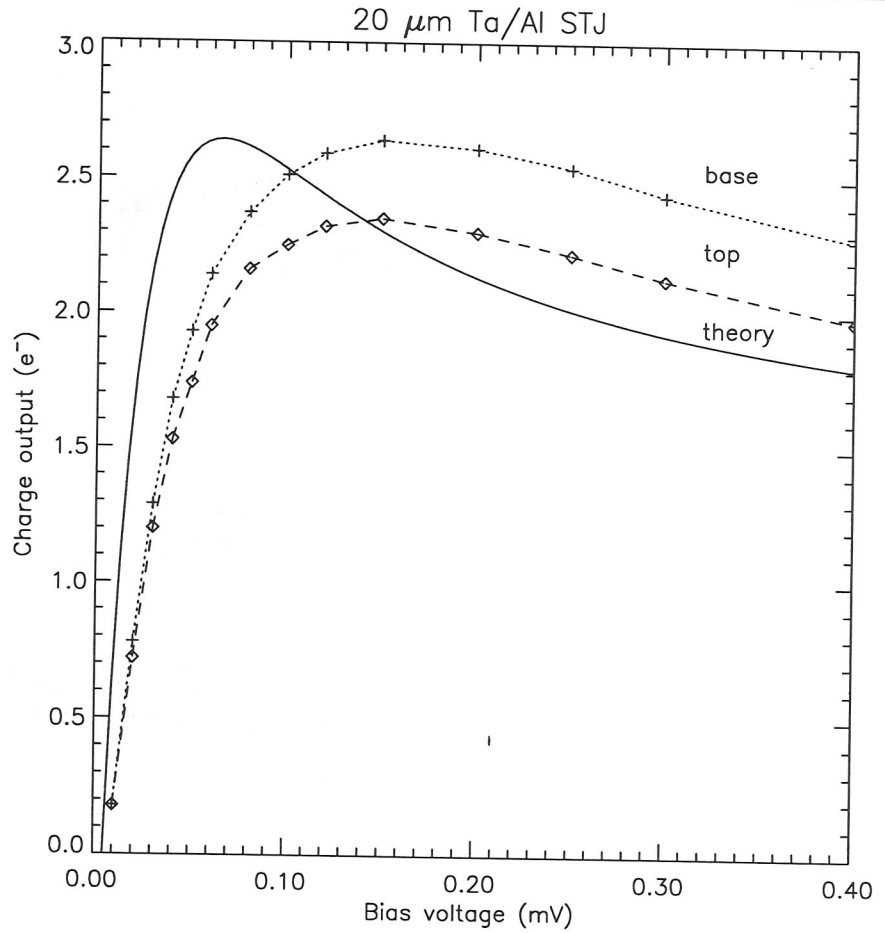

P. Verhoeve, priv. comm.

I-V curves: basic features and diagnostics

- Josephson current: I_J ($\leq I_{crit}$)
- Fiske steps @ V_{nm} (n,m = 0,1,2…)
- Subgap (= dark) current: I_{subgap}
- Gap voltage: $V_{gap} = 2\Delta_{gap}/e$
- Dynamic resistance: R_D
- Normal resistance: R_N

Basic subgap diagnostics:

- Leakage current
- Magnetic flux-trapping

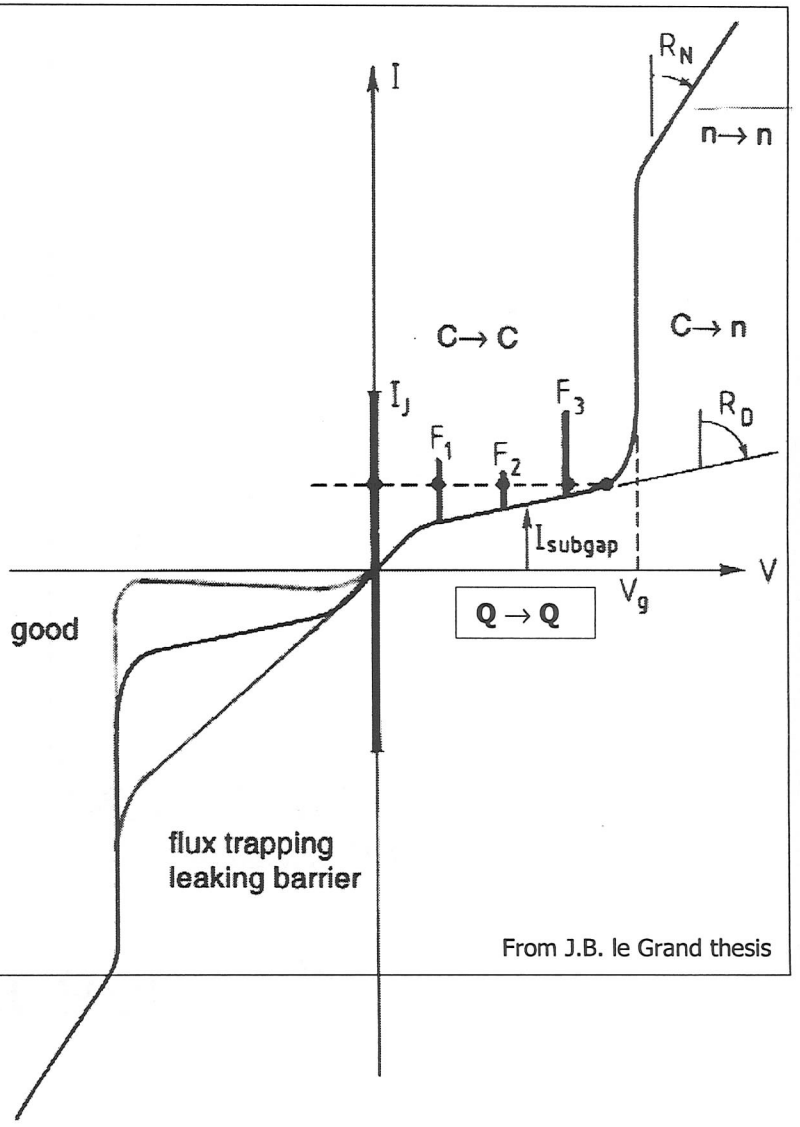

From J.B. le Grand thesis

I-V curves: Josephson effect and suppression

- Josephson effect:

$$I_J = I_{crit}\sin\phi; \quad \frac{d\phi}{dt} = 2\pi\nu_J; \quad \phi(t) = \phi_0 + 2\pi\nu_J t$$

$$\nu_J = \frac{V}{\Phi_0} \equiv 483.6\,\text{MHz}\left(\frac{V}{\mu V}\right) \qquad \begin{array}{l} V=0 : DC \\ V\neq 0 : AC, \langle I_J\rangle = 0 \end{array}$$

$$\Phi_0 = \frac{h}{2e} \equiv 2.06810^{-15}\,\text{Wb}$$

- Fiske steps:
  non-linear interaction between AC J current and 2-D EM cavity modes in barrier
- Coupling with magnetic field in barrier:

$$\nabla_{x,y}\phi = \frac{2\pi(2\lambda_L + d)}{\Phi_0}\vec{B}\times\hat{e}_z$$

- Suppression:

$$I_{crit}(B) = I_{crit}(0)\ \text{sinc}\left(\pi\frac{\Phi}{\Phi_0}\right) \qquad \begin{array}{ll} \propto |B|^{-1} & \text{square} \\ \propto |B|^{-2} & \text{diamond} \end{array}$$

Simultaneous suppression of I_J and Fiske steps is impossible

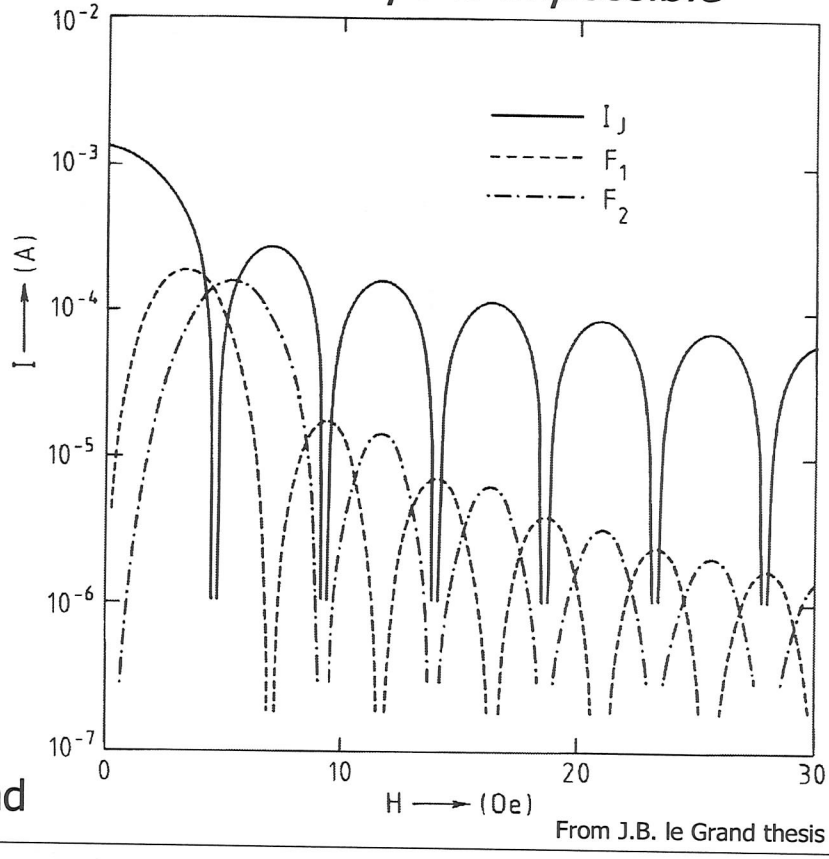

From J.B. le Grand thesis

I-V characteristics: basic expressions

Expression:

N_0: single-spin normal-state D.O.S.
ε_r: relative dielectric constant
λ_L: London penetration depth

$$V_{\text{gap}} = 2\Delta_{\text{gap}} / e$$

$$R_N(T \to 0) = \left[e^2 N_0 \langle v_\perp \rangle A P_{\text{tun}}\right]^{-1}$$

$$I_{\text{crit}}(T \to 0) = \frac{\pi}{4} \frac{V_{\text{gap}}(0)}{R_N}$$

$$V_{nm}^{\text{F}} = \frac{hc}{4e}\left(\frac{d}{\varepsilon_r(2\lambda_L + d)}\right)^{1/2}\left(\frac{m^2}{L^2} + \frac{n^2}{W^2}\right)^{1/2} ; \quad A = L \times W$$

$$I_{\text{sg, BCS}} = \frac{\left[\Delta_g + eV_b\right]\left[2\pi\Delta_g kT\right]^{1/2} e^{-\frac{\Delta_g}{kT}}}{eR_N\left[\left(\Delta_g + eV_b\right)^2 - \Delta_g{}^2\right]^{1/2}} \propto A P_{\text{tun}} T^{1/2} e^{-\frac{\Delta_g}{kT}}$$

$$kT << eV_b < 2\Delta_g$$

Tunnel process:	Meas. values Ta, 25 x 25 μm^2
C → n	0.65 mV
n → n	0.4 Ω → $P_{\text{tun}} \approx \frac{1}{8000}$
C → C	2.5 mA
C → C	V_{01} = 0.3 mV
Q → Q	~ few pA (T=0.3 K, IR shielding)

I-V curves: photon detection

$$Q_{\text{out}} = \int_0^{\infty} dt \left[I_{\text{tun}}(t) - I_{\text{sg}} \right] = \left\langle n_{\text{tun}} \right\rangle \frac{E_{\text{photon}}}{1.75\Delta}$$

$$\frac{\text{Signal}}{\text{Noise}} = \frac{Q_{\text{out}}}{\tau I_{\text{sg}}} = \frac{6000\, e/\text{eV}}{7\,\mu\text{s} \cdot 60\,\text{pA}} \cong 2\,\text{eV}^{-1}$$

Noise sources (I_{subgap}):

- thermally excited qps: $I \propto T^{1/2} \exp(-\Delta/kT)$

  $\Rightarrow$ $T_{\text{oper}} << T_{\text{crit}}$
- leakage
- IR background
- microphonic coupling
- electronics

Other quality definitions: $R_D/R_N \approx 3.5\ 10^6$

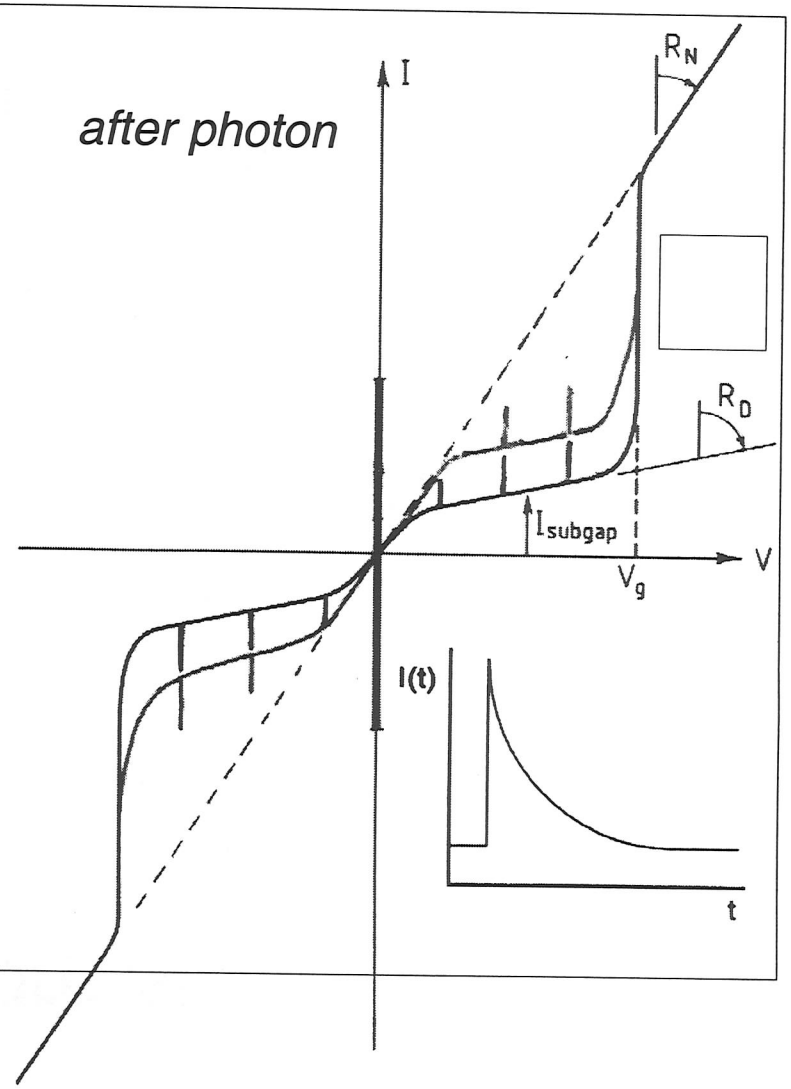

Photon-absorption

- Optical - UV:
  direct interaction between photon and conducting e^- in Cooper pair
  $\rightarrow$ energetic qp
- X-ray:
  photon is captured in atomic shell and ejects primary $e^- \rightarrow$
  secondary $e^- \rightarrow \Omega_{Debye}$ phonons $\rightarrow$ energetic qps

Energetic qp cascades down to a cloud of qps with energies $\sim\Delta_{gap}$
via interaction with phonons

QPs & phonons

Processes:	timescale
• QP tunneling → I_{tun}	few μs
• QP recombination → *non-linearity*	ns – ms
• QP losses → ΔE *degradation*	few μs
• Phonon transmission → *no* I_{tun}	ns
• Phonon pair-breaking → *primary & fastest process*	1 - 10 ps
• Phonon losses → *eff. qp loss*	ns

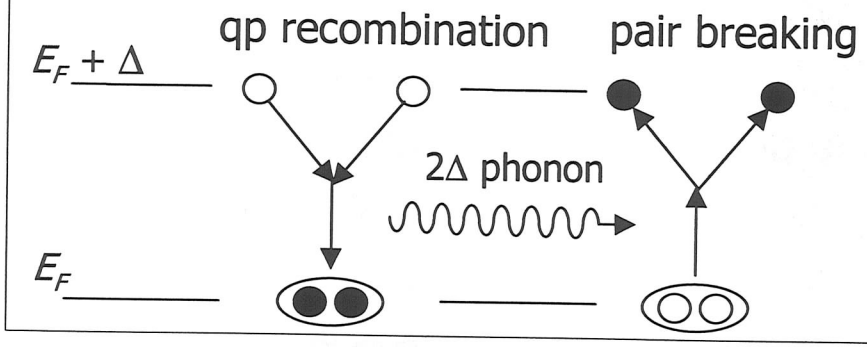

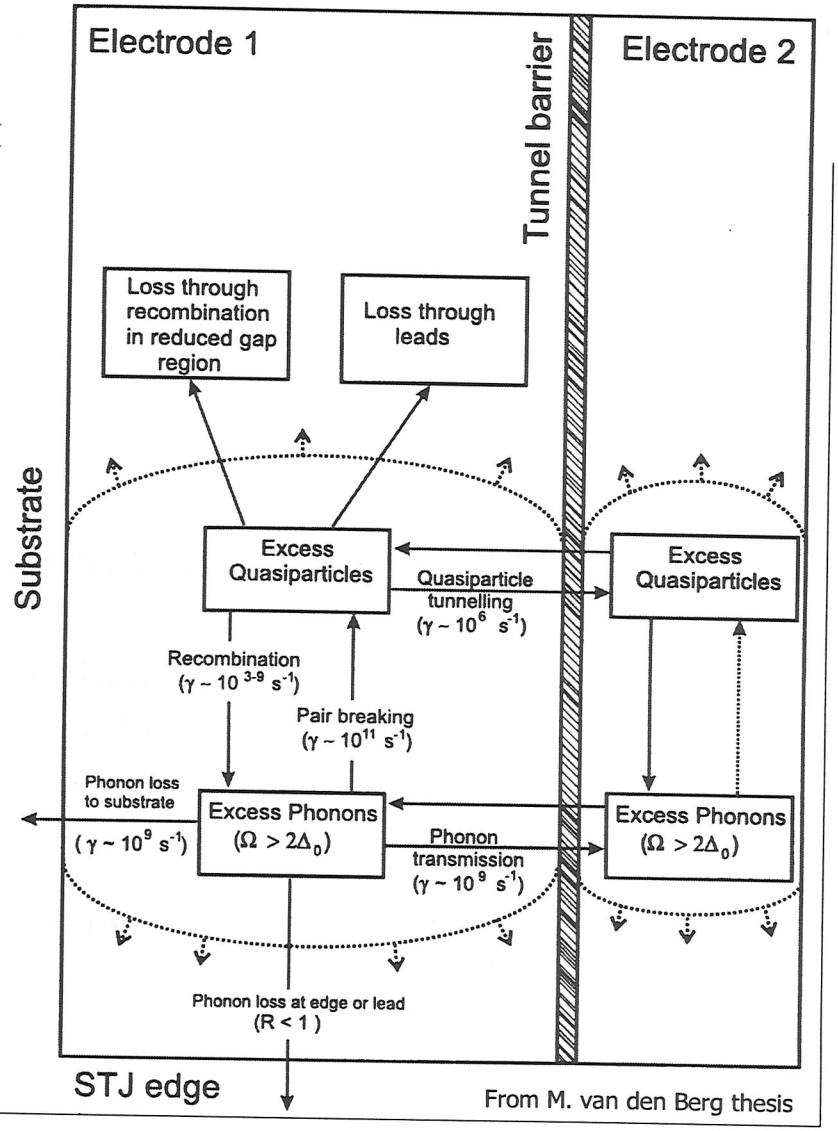

Rothwarf-Taylor equations

$$\frac{dn_{qp}^{i}}{dt} = -n_{qp}^{i}\left(\Gamma_{qp\,tun}^{i\to j} + \Gamma_{qp\,loss}^{i} + \Gamma_{ph\,trans}^{i\to j} + \Gamma_{ph\,loss}^{i}\right) + n_{qp}^{j}\left(\Gamma_{qp\,tun}^{j\to i} + \Gamma_{ph\,trans}^{j\to i}\right)$$

i, j = top, base; Γ=probability per time unit

refs.: A. Rothwarf and B.N. Taylor, PRL 19, 27 (1967)
P. Verhoeve et al., PRB 53, 809 (1996)

- Pair-breaking is 100 - 1000 times faster than qp recombination $\Rightarrow$ phonon population closely coupled to qps; no separate eq. needed
- RT equations should be augmented with diffusive term of form $-D\,\nabla^2 n_{qp}$
- RT equations are non-linear due to qp self-recombination:

$$n_{qp}^{i}\Gamma_{qp\,rec}^{i} = R\left(n_{exc}^{i} + \cancel{2n_{th}^{i}}\right)^2; \quad R = \frac{1}{4N_0\Delta\tau_0}\left(\frac{2\Delta}{kT_C}\right)^3\left(\frac{\Gamma_{ph\,trans}^{i\to j} + \Gamma_{ph\,loss}^{i}}{\Gamma_{PB}^{i}}\right)$$

$T \ll T_C$

Proximity effect in practice...

- Electrical contact between two different superconductors mutually influences
  Δ (pair potential) and N (density of states)
- Range: a few coherence lengths ξ

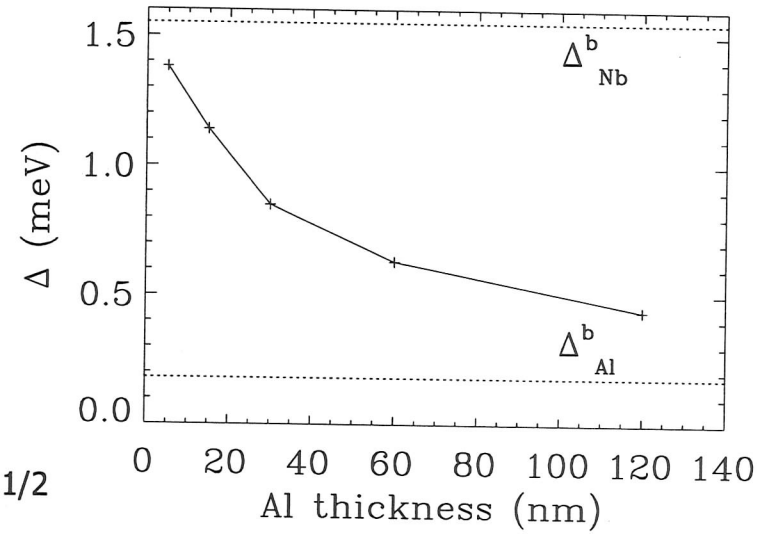

Two limiting regimes:

- Dirty limit: $\lambda_{mfp} < \xi < d \rightarrow \xi = [\frac{1}{3} \lambda_{mfp} \xi_{bulk}]^{1/2}$
- Clean limit: $\lambda_{mfp} > \xi > d \rightarrow \xi^{-1} = \lambda^{-1}_{mfp} + \xi^{-1}_{bulk}$

in vertical direction: $\lambda_{mfp} \approx d \rightarrow$ dirty limit

in lateral direction: $\lambda_{mfp} \approx$ 40 nm (poly)
few μm (epi)

ξ typically 100 nm

Note: in proximified structures, the pair potential Δ is not the same as gap energy Δ_{gap}

Ref.:
A. Poelaert et al., Proc SPIE v2808, 1996

... and theory

Proximity effects at an S'/S interface are best described using Usadel's equations for functions F(x,ε) and G (x,ε), where Re F = CP d.o.s. and Re G = QP d.o.s.

$\Rightarrow$ pair potential $\Delta(x)$

Input parameters:

$$\gamma = \frac{\rho_{S'}\xi_{S'}}{\rho_S\xi_S} = \frac{\sqrt{D_{S'}}N_{S'}}{\sqrt{D_S}N_S}$$

$$\gamma_{BN} = \frac{R_{intf}}{\rho_S\xi_S}$$

Ref.:

K. Usadel, PRL 25, 507 (1970)

A. Golubov et al., PRB 51, 1073 (1995)

S. Gueron, CEA Saclay PhD thesis (1998)

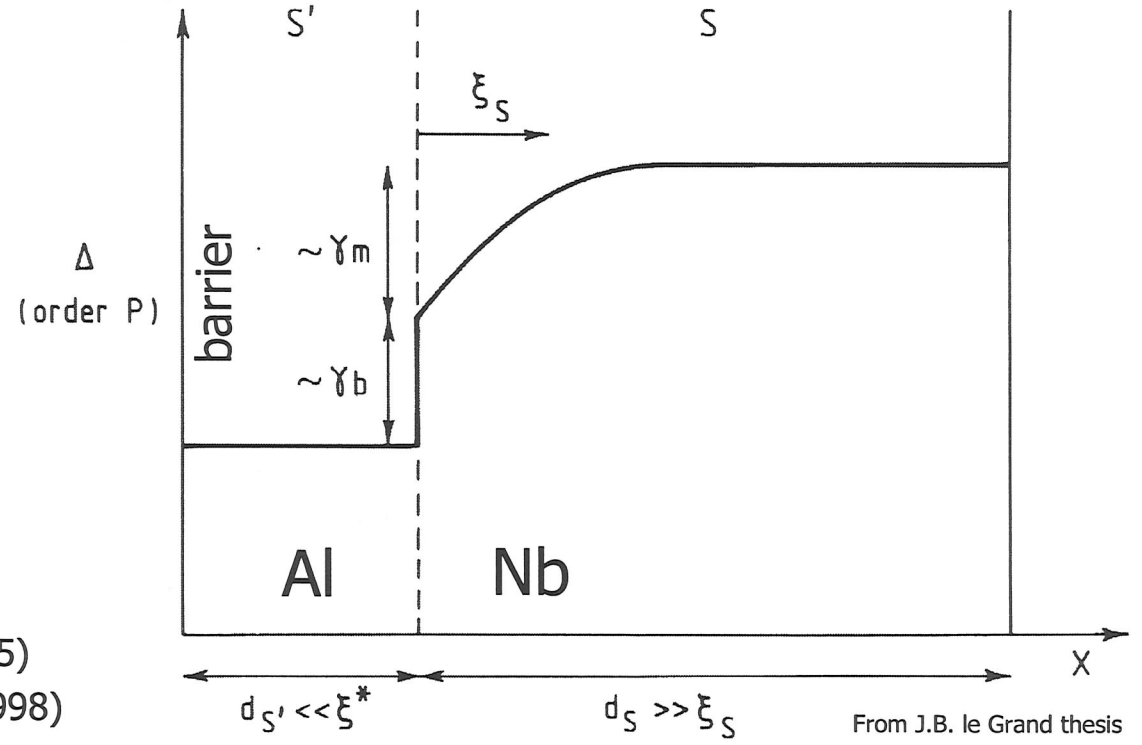

From J.B. le Grand thesis

QP confinement in trapping layers ?

- Layer thicknesses only few coherence lengths ξ :
  $\Rightarrow$ Pair potential Δ changes with height, but not Δ_{gap}
- QP density of states changes across Nb/Al interface:
  - QPs are concentrated close to the barrier due to the local availability of quantum states there
  - Andreev reflections help to confine low-energy qps to the Al layer

  $\Rightarrow$ enhanced tunneling probability with Al thickness

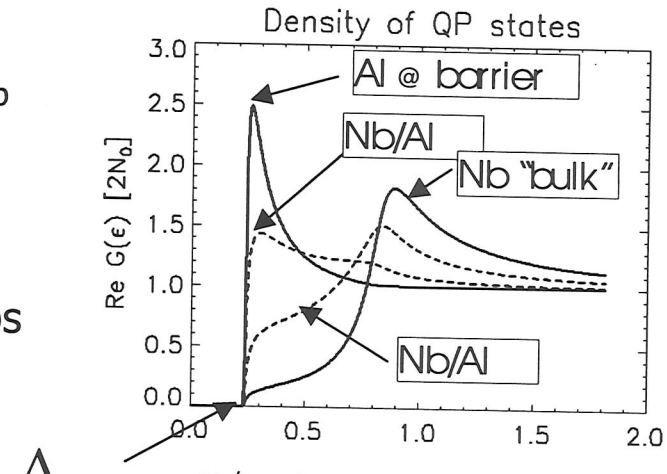

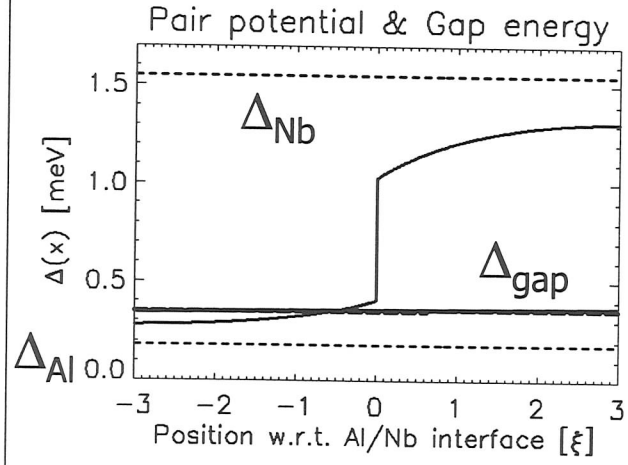

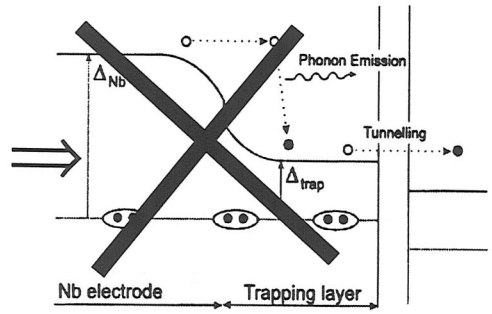

See A. Poelaert's thesis

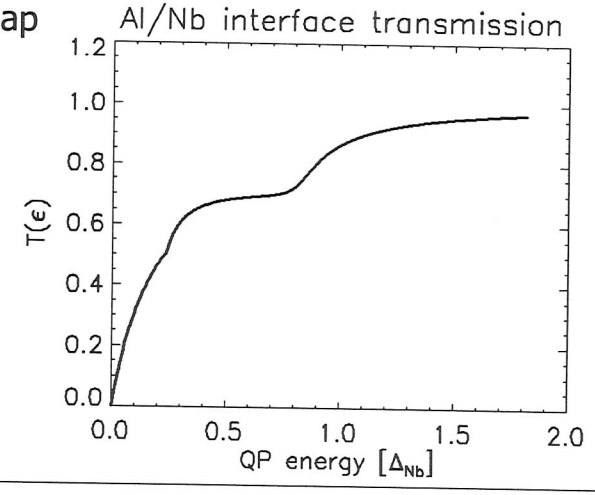

QP trapping in local sites

Lateral dimensions » ξ

- Δ_{gap} changes with lateral position, e.g. near NbO pockets at edge
- QPs are trapped in low-Δ region after emission of phonon with energy $\Omega > \Delta_0 - \Delta$
- De-trapping occurs after absorbtion of phonon:

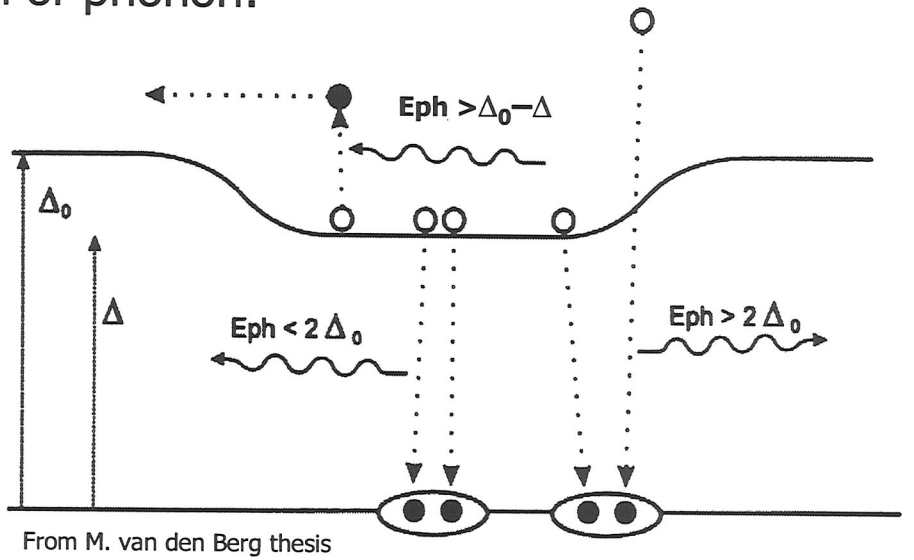

From M. van den Berg thesis

QP balance energy

- QPs gain energy eV_b by one tunnel + backtunnel process
- QPs gain energy by absorbtion of phonons
- QPs loose energy by emission of phonons (excl. recombination)
- Phonon emission and absorption rates Γ_{em} and Γ_{abs}, and tunnel rate Γ_{tun}, depend strongly on qp energy

$\Rightarrow$ A balance energy $E_{bal} > \Delta_{gap}$ exists such that $\Gamma_{tun} + \Gamma_{abs} = \Gamma_{em}$

- E_{bal} depends on V_b

$$\Rightarrow Q_{out} = \langle n_{tun} \rangle \frac{E_{photon}}{1.75 E_{bal}}$$

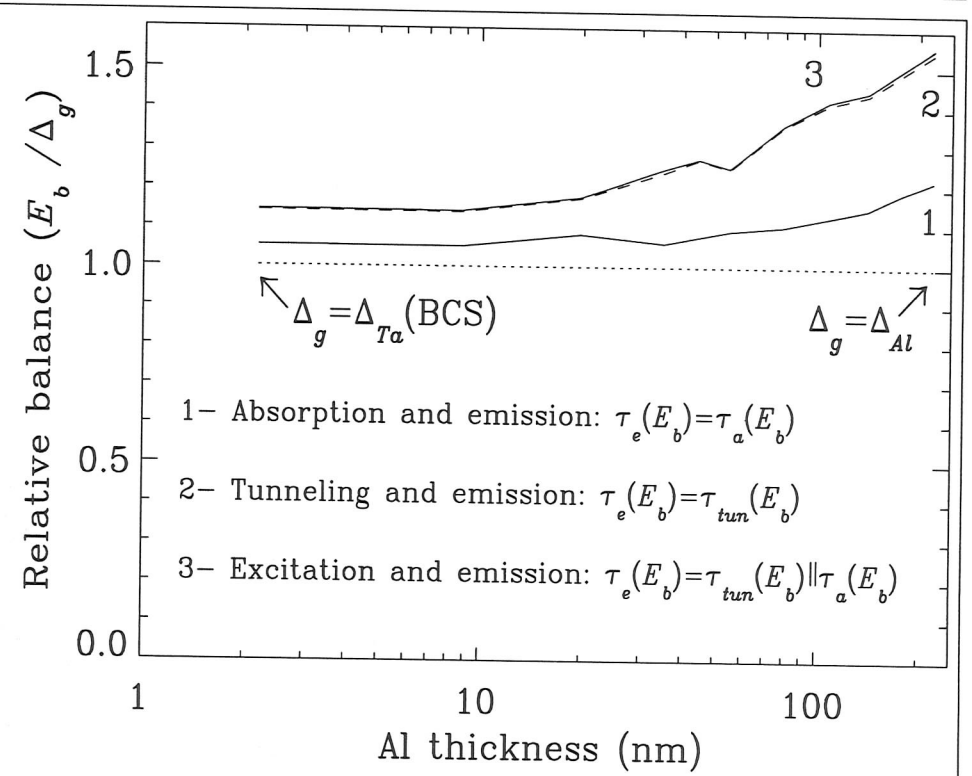

Refs.:

S. Kaplan et al., PRB 14, 4854 (1976)
A. Poelaer et al., Proc. LTD8, in press

STJ spectroscopy: examples

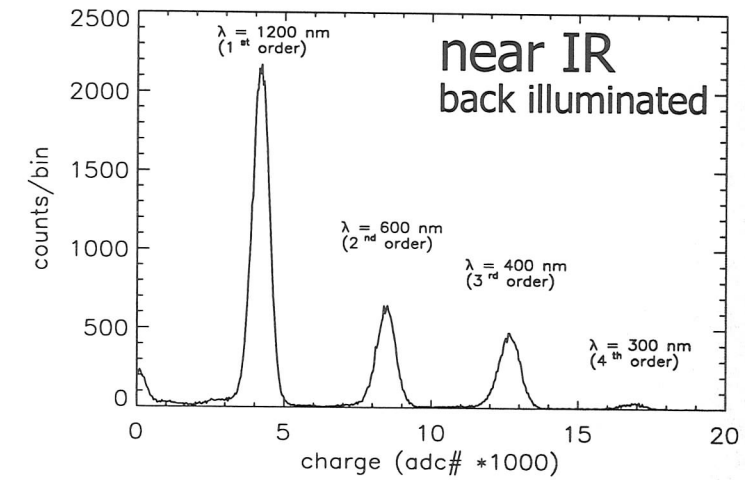

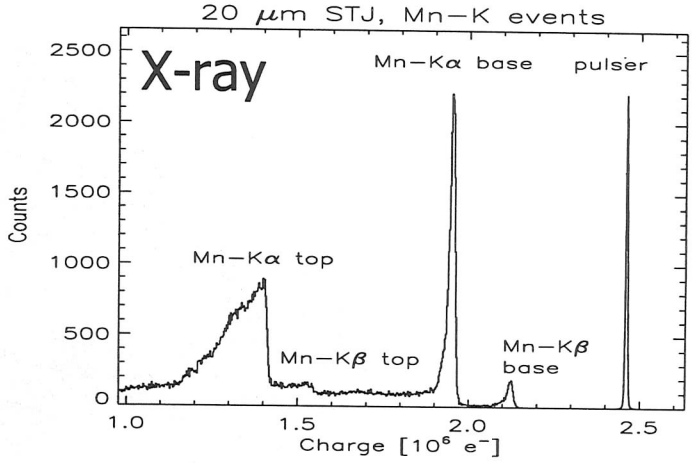

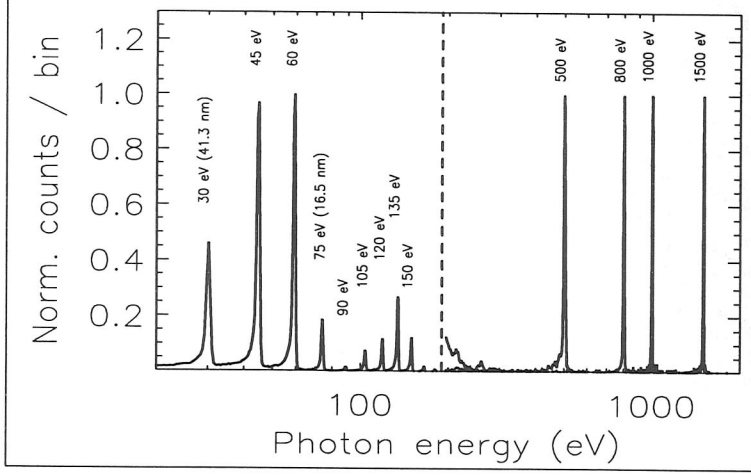

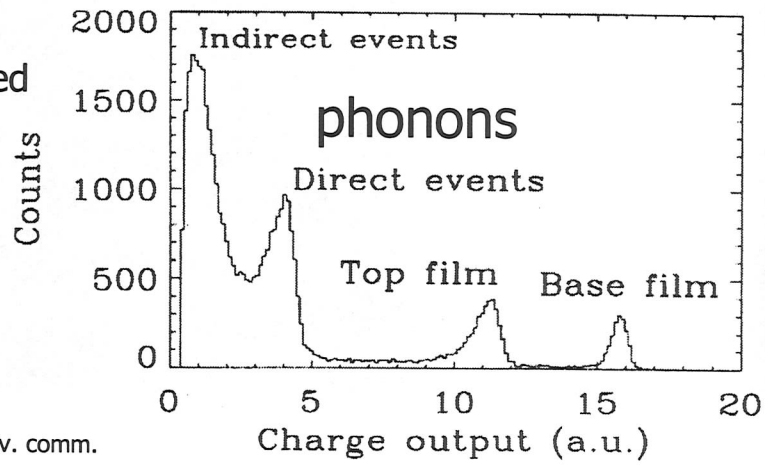

P. Verhoeve, priv. comm.

STJ spectroscopy: spectral features

Vertical: # counts

X-axis: Q_{out}

Y-axis: τ_{pulse}

Features:

- substrate events
- primary e^- across barrier
- events with qp loss

P. Verhoeve, priv. comm.

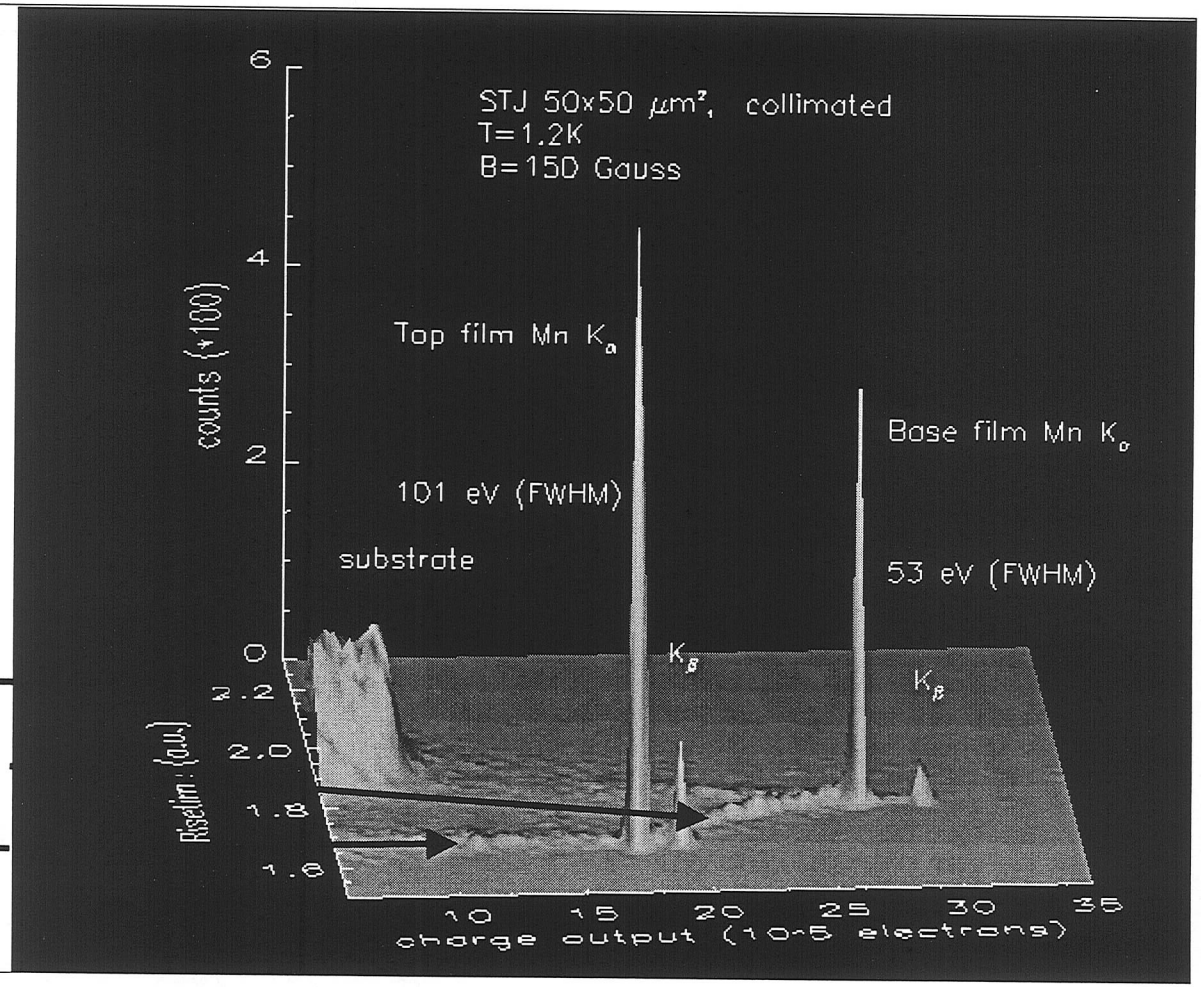

STJ spectroscopy: energy resolution in practice...

Best 5.9 keV energy resolutions				
Group	Material	FWHM (eV)		QE
		meas.	limit	
LNLL	Nb / Al	29	10.	5%
ESTEC	Ta / Al	16*	6.7	5%
Univ. of Munich	Al	9.7	3.5	1%

*) Collimated to 10 μm beam

- Up to 1 keV ΔE cf. statistical limit
- Above 1 keV ΔE degrades $\propto E$

  Very difficult problem to solve!

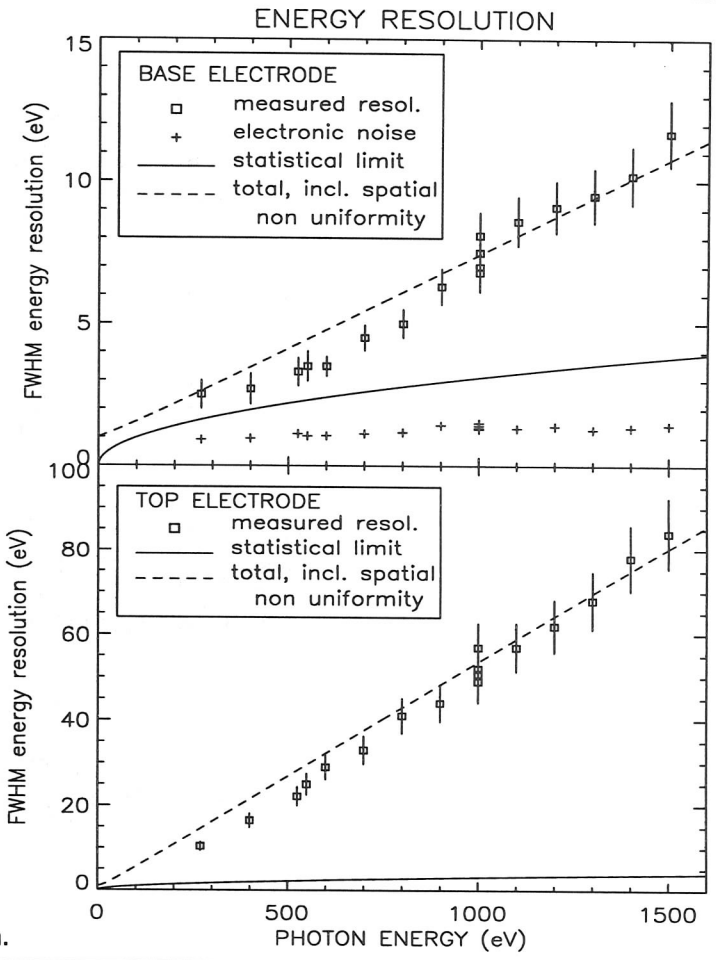

P. Verhoeve, priv. comm.

... and theory:

$$\Delta E(\text{fwhm}) = 2.355 \sqrt{\sigma_{\text{el}}^2 + \underbrace{\sigma_{\text{Fano}}^2 + \sigma_{\text{tun}}^2}_{\text{Statistical limit}} + \sigma_{\text{spat}}^2 + \ldots}$$

- σ^2_{el}: noise contribution from electronics. Monitored with pulser. Subtracted to obtain internal energy resolution.
- $\sigma^2_{\text{Fano}} = F\,\varepsilon\,E$, with Fano factor $F = 0.22$: Poissonian noise on initial number of qps
- $\sigma^2_{\text{tun}} = G\,\varepsilon\,E$, with $G = 1 + \langle n_{\text{tun}} \rangle^{-1}$: Poissonian noise on number of tunneling qps
- $\sigma^2_{\text{spat}} \propto E^2$ contribution from spatial non-uniformity in charge response
  Potential sources: losses in leads, local traps at edges,...
  Magnitude: 0.3 – 1 % $\rightarrow$ response surface

Refs.:

U. Fano, Phys. Rev. 72, 26 - 29 (1947)

N. Rando et al., NIM A 313, 173 (1992)

D. Goldie et al., Appl. Phys. Lett. 64, 3169 (1994)

P. Verhoeve et al., PRB 53, 809 (1996)

STJ spectroscopy: response surface

Low Temperature Scanning Electron Microscopy

- STJ's response surface is scanned with narrow (0.1 μm) e^- beam.
- In theory, σ_{spat} can be obtained directly from surface fluctuations
- QP diffusion into leads tend to dominate spatial non-uniformities
- Enhanced qp recombination at edges?
- Looking for 0.5% fluctuations is at limit of instrument

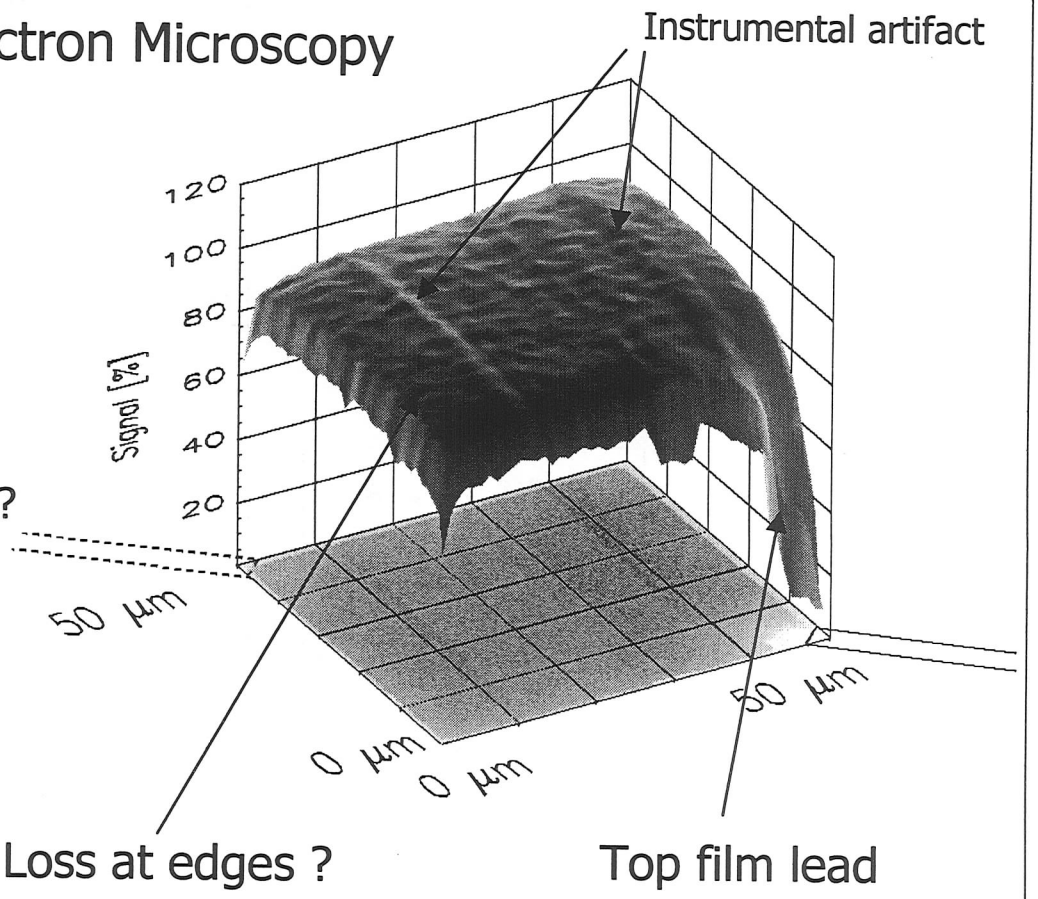

J.B. le Grand, priv. comm.

STJ spectroscopy: the SRON model

A model for spatial inhomogeneities

SRON model solves diffusion equation for qp density to obtain STJ response surface:

$$\frac{\partial n}{\partial t} = D\nabla^2 n - \left(\Gamma_{\text{tun}} + \Gamma_{\text{loss}}\right)n$$

and boundary conditions that assume non-ideal edges (reflectivity $R < 1$).

- Model explains, at least qualitatively, relation between ΔE and STJ size
- QP diffusion does play a role!

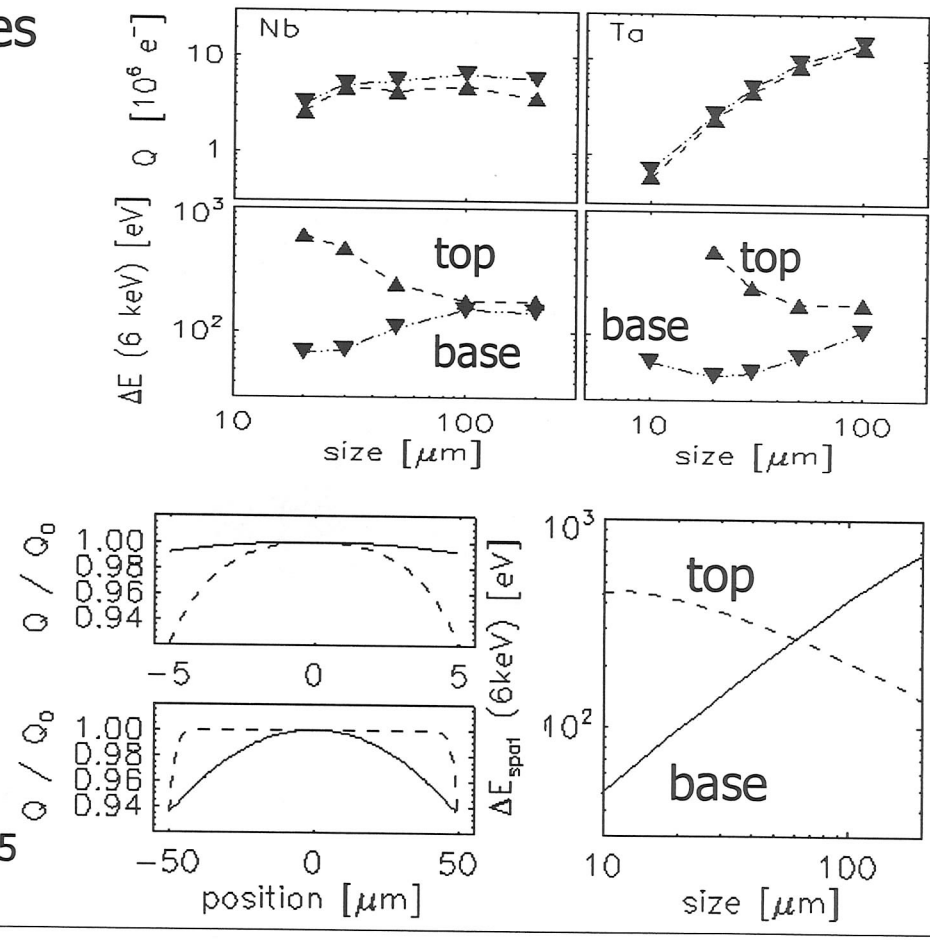

Refs.:

O.J. Luiten et al., *Proc. of LTD-7,* Munich 1997, 25
M. van den Berg, PhD thesis, Univ. Utrecht, 1999

STJ spectroscopy: summary

- Best ΔE still factor 3 worse than statistical limit
- Problem is generally attributed to spatial non-uniformity of response
  Potential causes:
  - QP losses down leads → solved by using high-Δ leads
  - QP trapping at edges → thin metal-oxide layers acquire zero Δ
  - Enhanced recombination at edges → requires accurate phonon parameters
  - Spatial fluctuations in barrier transmissivity
- Alternative explanations:
  - Underestimation of electronic noise by pulser, due to bias instability
  - Low-frequency bias instability that influences initial number of QPs
- Problem is how to disentangle different effects

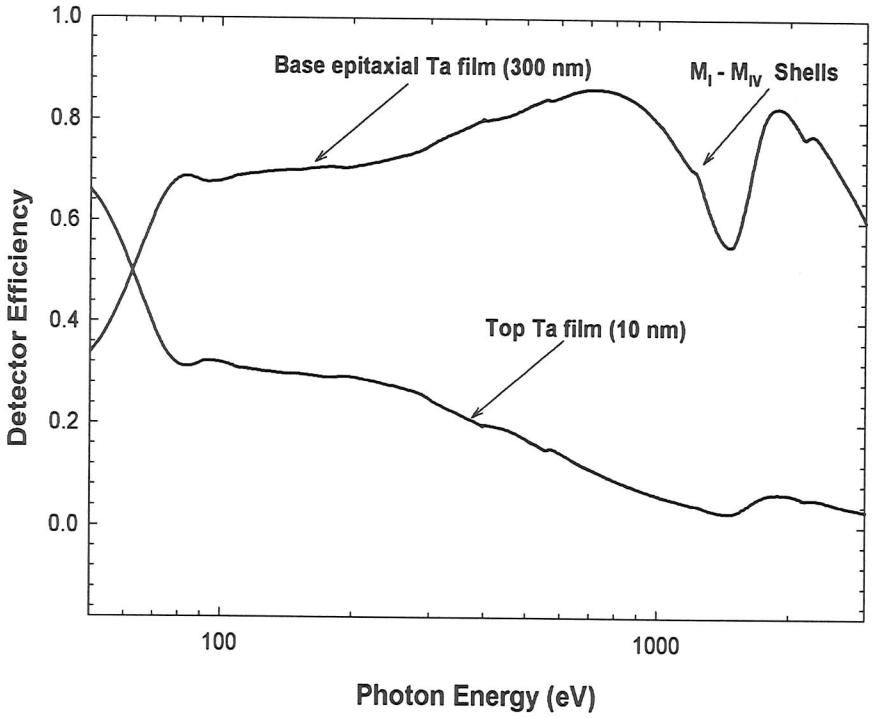
Base epitaxial Ta film (300 nm)
M_I - M_{IV} Shells
Top Ta film (10 nm)
Detector Efficiency
Photon Energy (eV)
1.0
0.8
0.6
0.4
0.2
0.0
100
1000

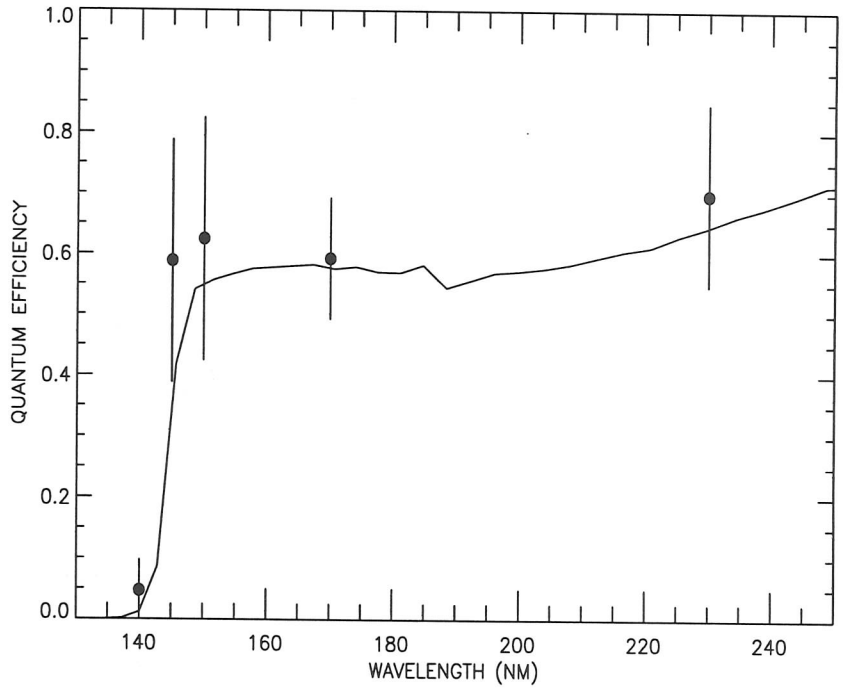
QUANTUM EFFICIENCY
WAVELENGTH (NM)
1.0
0.8
0.6
0.4
0.2
0.0
140
160
180
200
220
240

New developments: S-Cam array

Optical camera, containing a 6x6 array of 25 μm Ta/Al STJs, succesfully operated at the 4.2 m William Herschel Telescope at La Palma, Canary Islands

Specifications:

- Nominal band-pass: 350 – 650 nm
- Intrinsic ΔE =0.14 eV @ 2.5 eV = 500 nm $\rightarrow \lambda / \Delta\lambda = 18$
- Effective ΔE =0.5 eV $\rightarrow \lambda / \Delta\lambda = 4$ due to electronic noise (1200 e^- rms) and pile-up due to thermal IR background
- Time accuracy: 5 μ s
- Max. countrate per pixel: 1 kHz
- Plate scale: 0.6 arcsec / pixel

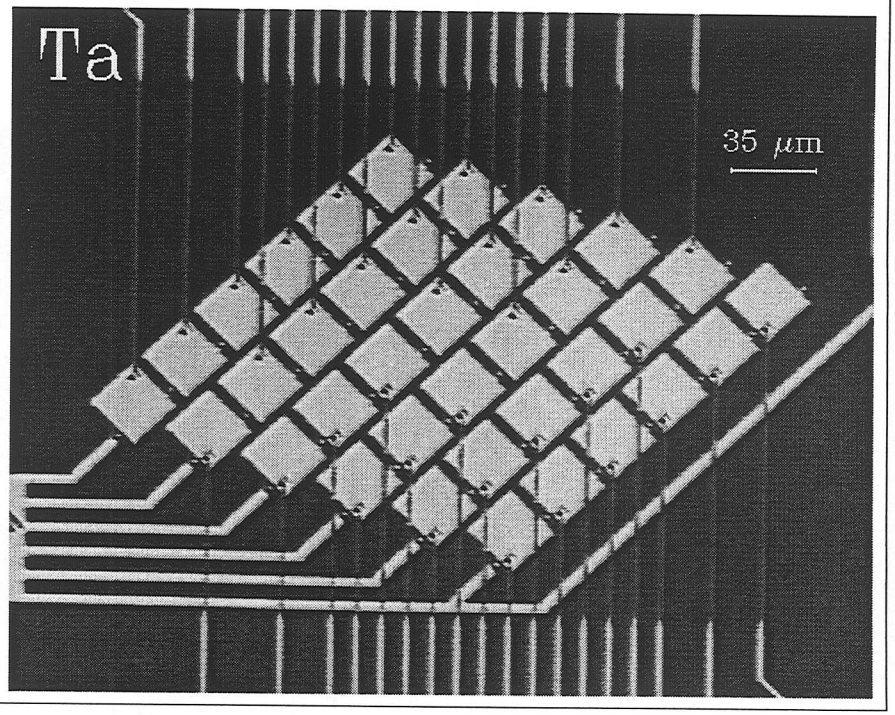

Ref.:

N. Rando et al., *Proc. LTD-8*, Dalfsen, 1999

New developments: X-ray imaging spectroscopy

4 Ta/Al STJs on Ta absorber:
200 x 200 x 0.1 μm³

$\Delta E \geq 32$ eV @ 6 keV

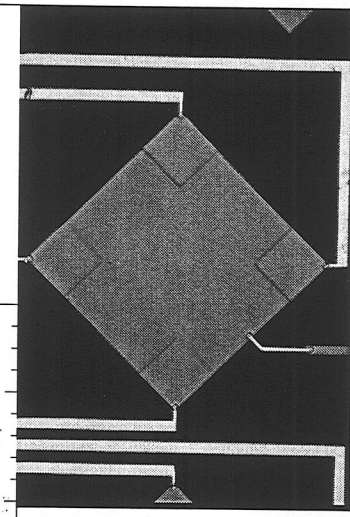

Fraunhofer diffraction:
$\Delta x \approx 10$ μm

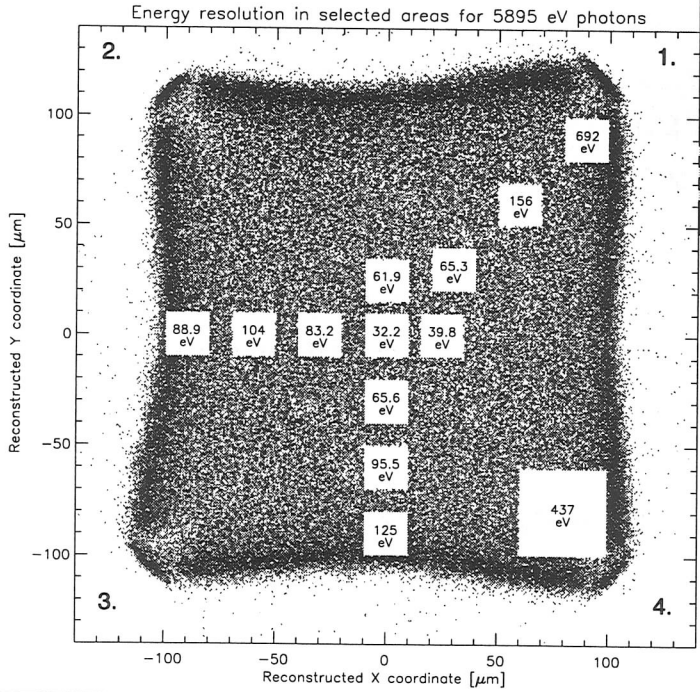

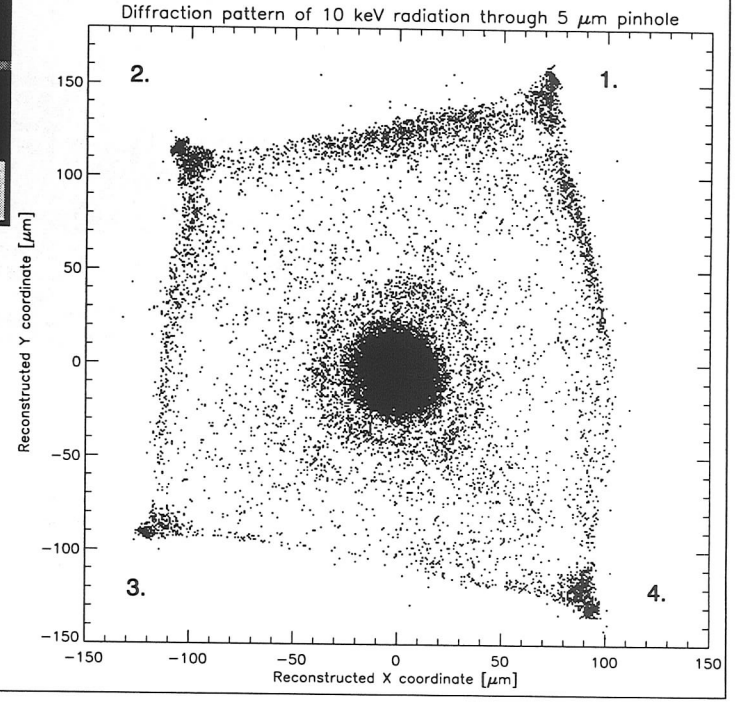

New developments: sub-mm single photon det.

Photons with frequencies between 100 GHz ($2\Delta_{Al}$) and 700 GHz ($2\Delta_{Nb}$) will break CPs in Al absorber.

Tunnel current across STJ is measured with the RF-SET

Promised detector properties:

- Read-out bandwidth > 10 MHz
- Responsivity 5000 A/W
- Response time < 1 μ s
- Predicted NEP < 3 10^{-20} $WHz^{-\frac{1}{2}}$

Ref.:

R. Schoelkopf et al., Proc. ASC 1998
IEEE Appl. Superc. 9, 2935 (1999)

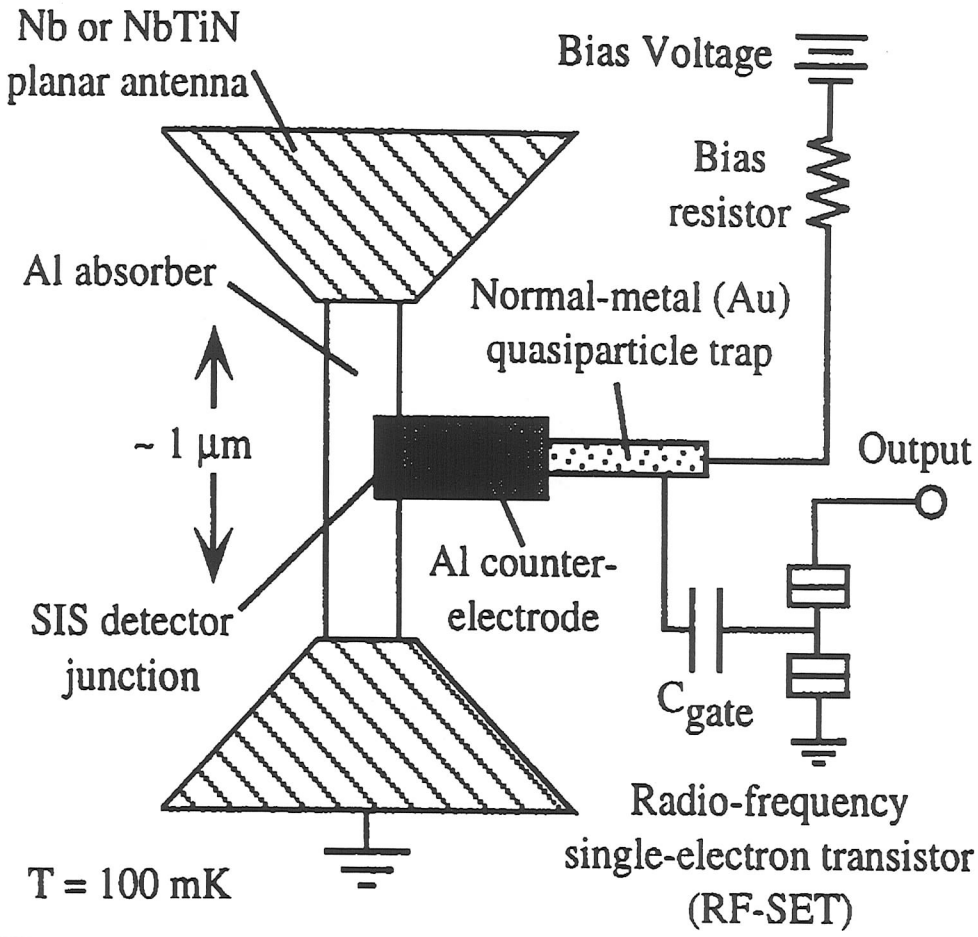

New developments: new materials

$$\Delta E_{stat} \propto \sqrt{\Delta_{gap}}$$

mat.	Δ_{gap} [meV]	Δ_{gap} [GHz]	T_{crit} [K]
Nb	1.55	375	9.25
Ta	0.664	161	4.47
Al	0.179	42	1.18
Mo	0.139	32	0.92
Hf	0.0194	4.6	0.13
W	0.003	0.72	0.015

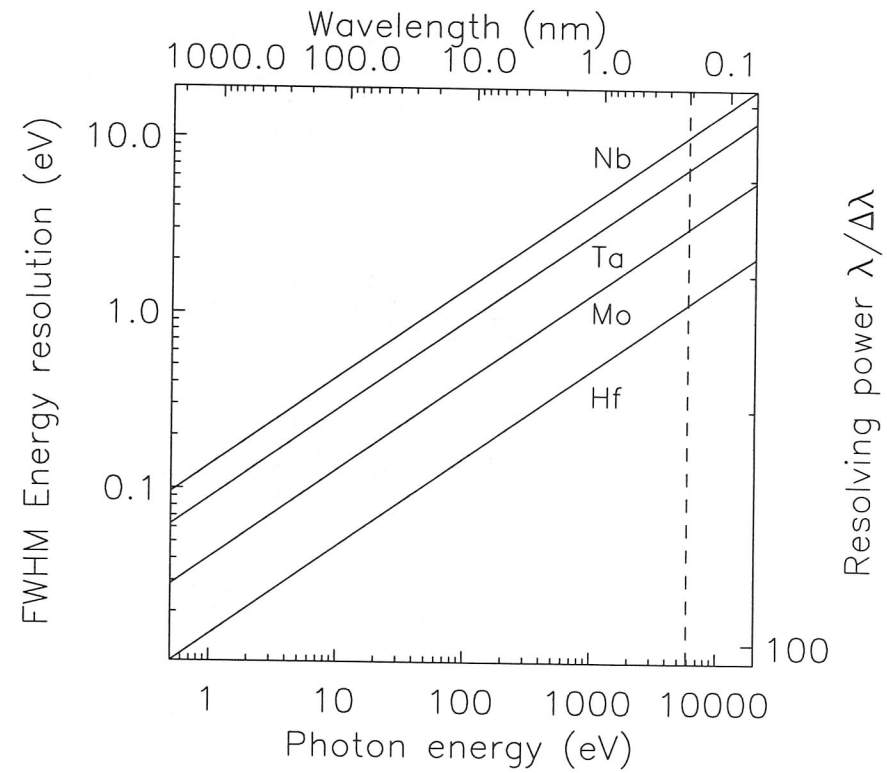

New developments: matrix read-out

- Wiring problem becomes prohibitive for large format arrays
- Matrix read-out provides √N reduction
- Limit is given by series noise from combined capacitors (STJs)

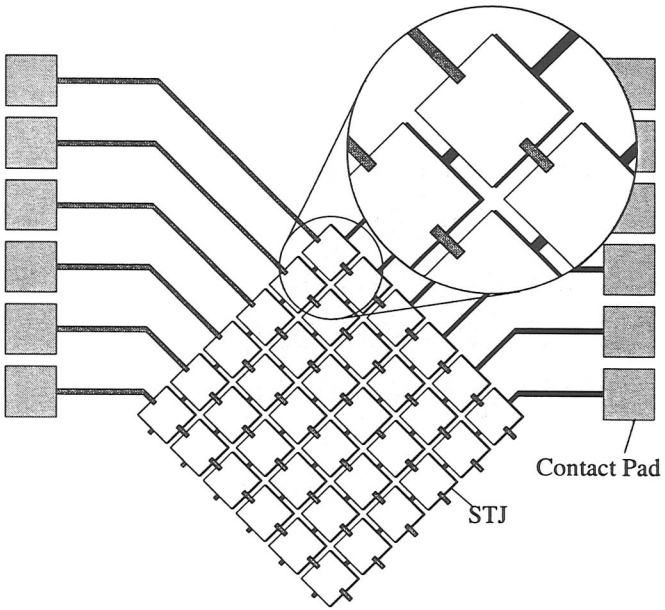

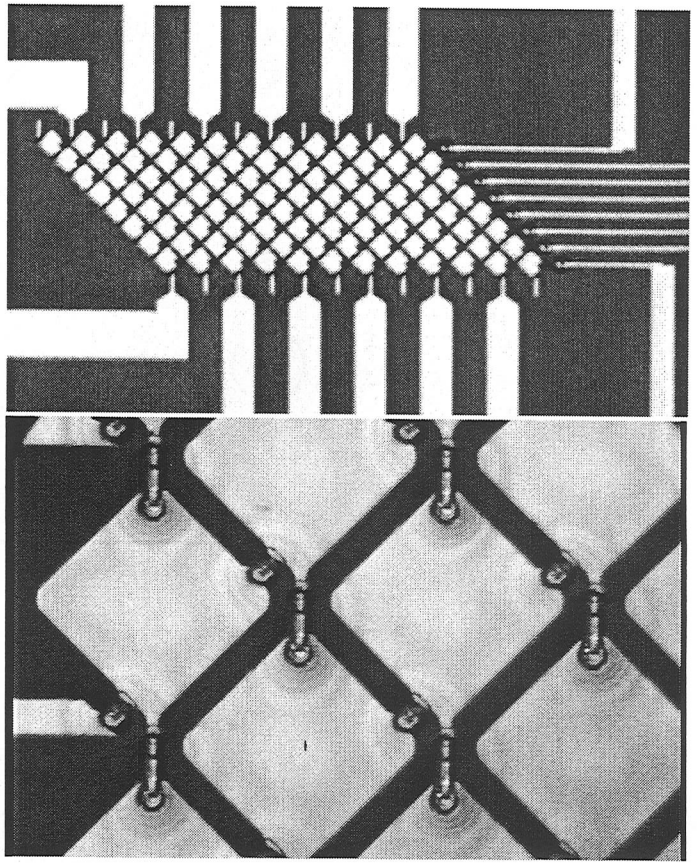

Ref.: D. Martin et al., *Proc. LTD-8*, Dalfsen, 1999

STJ read-out: charge vs. current-sensitive amp.

Charge-sensitive:

+ simpler electronics for pulse shaping
+ fast (on-line integration and filtering)
+ large numbers of pulses
+ biasing more stable
– only optimal for one shape

Current-sensitive:

– pulse sampling fast digital oscilloscope
– slow (off-line integration and filtering)
– limited number of pulses
– biasing sensitive to current peaks
+ different pulse-shapes

Charge / current-sensitive amplifier

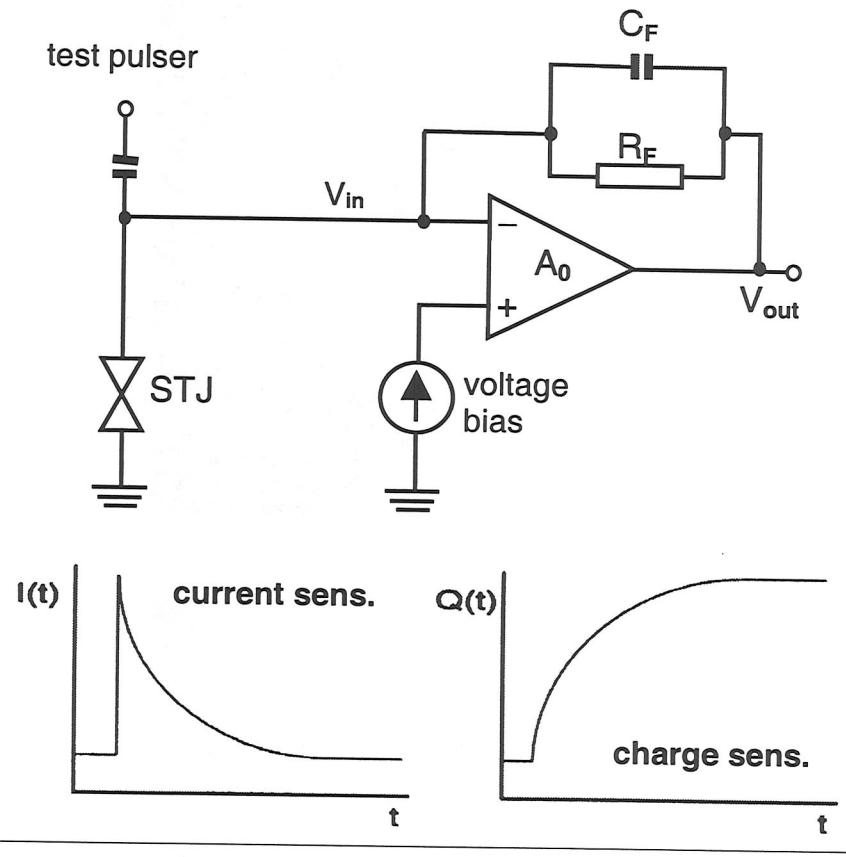

STJ read-out: biasing

- Bias shift:

$$V_{\text{in}} = \underbrace{\frac{A_0}{1+A_0} V_{\text{bias}}}_{DC} - \underbrace{\frac{Z_{\text{in}} I(\omega)}{1+A_0}}_{AC}$$

$$Z_{\text{in}} = \begin{cases} R_F & \text{current sens.} \\ \dfrac{R_F}{1 + j\omega R_F C_F} & \text{charge sens.} \end{cases}$$

- Current biasing is instable in presence of Josephson current or Fiske steps, (i.e. always)

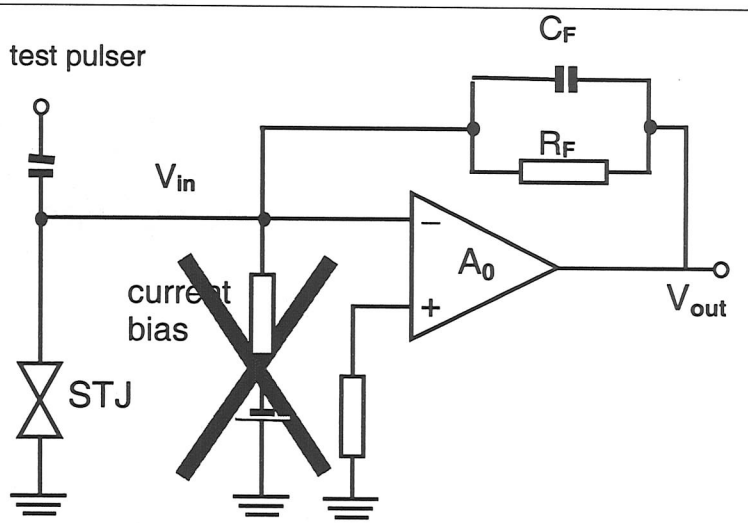

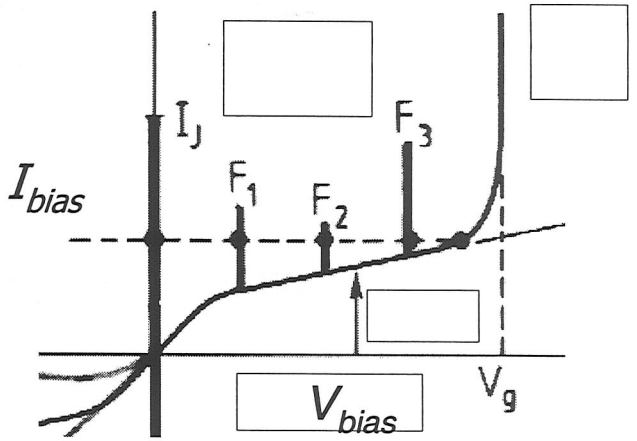

General References

- A. Barone & G. Paterno
  Physics and applications of the Josephson effect, J. Wiley & Sons NY, 1982
- M. Tinkham
  Introduction to Superconductivity, 2nd ed., Krieger FL, 1985
- J.B. le Grand
  X-ray response of Superconductive tunnel junctions with trapping layers
  PhD thesis, University of Utrecht, 1994
- C.P. Poole, H.A. Farach, R.J. Creswick
  Superconductivity, Academic Press Inc., 1995
- A. Poelaert
  Superconducting tunnel junctions used as photon detectors
  PhD thesis, University of Twente, 1999
- M. van den Berg
  Development of a High Resolution X-ray Spectrometer based on STJs
  PhD thesis, University of Utrecht, 1999

UV/Optical Imaging Spectroscopy with Cryogenic Detectors

ESLAB 1999/062/SA

IR Filters for High Responsivity Cryogenic Detectors

ESLAB 1999/063/SA

First Astronomical Results from S-Cam

ESLAB 1999/037/SA

New Readout Scheme for Superconduction Tunnel Junction Arrays

ESLAB 1999/067/SA

The Lateral Proximity Effect and Long-range Energy-gap Gradients in Ta/Al and Nb/Al Josephson Junctions

ESLAB 1999/064/SA

An X-ray Photon-counting Imaging Spectrometer based on a Ta Absorber with Four Superconduction Tunnel Junctions

ESLAB 1999/065/SA

Quasiparticle Energy Relaxation in Superconducting Tunnel Junction used a Photon Detectors

ESLAB 1999/066/SA

To be published in Proceedings of the 8th International Workshop on Low Temperature Detectors
Dalfsen - The Netherlands, 15-20 August 1999

Astrophysics Division - Space Science Department

European Space Agency
Agence spatiale européenne

ESTEC

UV/Optical Imaging Spectroscopy with Cryogenic

P. Verhoeve

ESA/ESTEC, Astrophysics Division, P.O.Box 299, 2200 AG Noordwijk, The Netherlands

ESLAB 1999/062/SA

To be published in Proceedings of the 8th International Workshop on Low Temperature Detectors
Dalfsen – The Netherlands, 15-20 August 1999

UV/optical imaging spectroscopy with cryogenic detectors

P. Verhoeve*

Space Science Department of ESA, Estec, P.O. Box 299, 2200 AG, Noordwijk, The Netherlands

Abstract

Recently, the photon counting capabilities of cryogenic detectors have been extended into the UV/visible/NIR spectral region. Superconducting Tunnel Junctions (STJ) as well as Transition Edge Sensors (TES) have shown single photon detection with moderate energy resolution well beyond λ=1 μm. They provide an excellent detection efficiency in the UV and visible (>50%) and high count rate capabilities. This allows for spectroscopic studies of weak sources or time-resolved studies of transient phenomena. These qualities make these detectors interesting alternatives to CCDs and micro-channel plates which are now the most commonly used detectors in UV/visible astronomy. While the present spectroscopic performance of single pixel STJs and microcalorimeters is already useful, it can be further enhanced by using lower T_c materials. The imaging properties, however, need to be much improved. Small prototype arrays of close-packed single STJs have been demonstrated, but large format arrays of individually connected STJs or microcalorimeters would be hampered by lack of cooling power, wire connection problems and massive electronics. Some solutions to this problem are discussed. An additional problem area is the detector's sensitivity in the IR: a large load of thermal IR radiation (e.g. from warm optics) will seriously degrade the spectroscopic performance. Sophisticated filtering is required to prevent this without loss in sensitivity.

1. Introduction

The present generation of detectors in UV/optical astronomy (λ~100-1000 nm or E=1.2-12 eV) is based on semiconductors (CCDs) or micro-channel plates (MCPs). CCDs combine large sensitive area (several cm^2) with high resolution imaging and excellent QE in the optical, but no photon-counting capability and marginal QE for λ<300 nm. In the UV, MCPs are most widely used because of the better QE of 10-40%, depending on wavelength and photo-cathode material. In addition, they provide photon-counting capability with time resolution <1 μs.

Recent developments in cryogenic detectors, such as superconducting tunnel junctions [1,2] (STJs) and microcalorimeters based on transition edge sensors [3] (TES), have added a third dimension to UV/optical detectors: simultaneous with the position information, they can provide each photon's arrival time and wavelength. Combined with their high detection efficiency (50-70% over the range λ~115-700 nm), this makes them the ideal detectors for applications such as fast spectro-photometry or deep-field imaging. Since these detectors have been packaged into arrays their existing performance may already be such that they could allow the simultaneous measurement of broad-band low-resolution spectra of very faint extragalactic sources to be obtained for all objects in the field. Such spectra containing emission line complexes or continuum absorption features (the Lyman edge) in very faint extragalactic objects may allow the direct determination of red-shifts [4,5]. Indeed, NASA's UV-Optical Working Group, which 'considers the next frontier in UV-optical space astronomy' proposes to use cryogenic detectors onboard a mission provisionally named ST2010 [6]. Possible configurations of cryogenic detectors on such a mission could be as echelle-spectrograph order-sorting devices in high-throughput UV spectroscopy, or in narrow-field imaging spectroscopy.

This paper intends to give an overview of the present status of cryogenic detectors for UV/optical applications, as well as to identify areas where further development is required and possible solutions to these problems.

2. Microcalorimeters/TES

A microcalorimeter generally consists of an absorber with heat capacity C, weakly linked to a heat sink via a thermal conductance g, and a thermometer (see Fig.1). When a photon is absorbed in the microcalorimeter, its energy will be thermalized, resulting in a rise of temperature which depends on the

* corresponding author: tel. +31-71-5655909, fax +31-71-5654690, e-mail pverhoev@estec.esa.nl

photon's energy. The thermometer can be a semiconductor thermistor or a superconductor held at its transition temperature T_c; a transition edge sensor (TES). A rise in temperature will change the thermometers's resistance, which is detected as a current pulse. TES are usually read out with arrays of dc SQUIDS used as current-sensitive amplifiers. The performance of micro-calorimeters has been significantly improved by using TES in electro-thermal feedback (ETF) mode [7] as thermometers. If the heat sink is cooled well below the T_c of the TES and the TES is voltage biased, the ETF will keep the TES stably at its superconducting transition. It also causes the TES to return much faster to its base T after the absorption of a photon: the effective time-constant for the detector becomes $\tau_{eff}=\tau_0/(1+\alpha/n)$, where $\tau_0=C/g$ is the intrinsic time constant, $\alpha=(T/R)(dR/dT)$ is a measure for the width of the superconducting transition, and $n=d(logP)/d(logT)$ (~5). In addition, the theoretical limit for the energy resolution of the detector becomes:

$$\delta E = 2.355[k_b T^2 C(8n)^{1/2}/\alpha]^{1/2}, \qquad (1)$$

which is independent of energy and can be lower than the thermodynamic limit for sufficiently large α. If the detector is optimized to be used up to a photon energy E_{max} without saturation [3], then $E_{max}\sim CT_c/\alpha$, and the energy resolution becomes:

$$\delta E = 2.355[k_b T_c E_{max}(8n)^{1/2}]^{1/2}. \qquad (2)$$

For a typical TES with T_c~80 mK, to be used in the UV and visible up to E_{max}=10 eV, the limiting resolution would be δE~0.05 eV.

Microcalorimeters operating in the UV/visible wavelength range have been reported by two groups. Both use the TES as absorber and thermometer simultaneously, in ETF mode with SQUID readout. Irwin et al. [8] used an Al/Ag bilayer with T_c=85 mK, 70x100 μm^2 and 50 nm thick, on a Si_3N_4 membrane. Heat pulses showed δE<0.2 eV for E=4 eV, with pulse decay times of 8 μs. No response to optical photons was reported.

Cabrera et al. [3] used a W TES with T_c=80 mK, 18x18 μm^2 and 40 nm thick, on a Si substrate. These devices achieve δE~0.15 eV for E=0.3-3.5 eV, with pulse decay times of 3-60 μs and rise times <0.5 μs [9]. The measured resolution is about a factor of 4 above the theoretical limit, which is partly due to phonon loss into the substrate. A migration to Si_3N_4 membranes as substrates is foreseen to reduce these losses and improve the energy resolution. Work is in progress to eliminate spectral contaminations due to photons absorbed in the Al contact wires. These devices have been used as single element detectors in a ground-based experiment to record simultaneously the light curve and spectrum of the Crab pulsar [9].

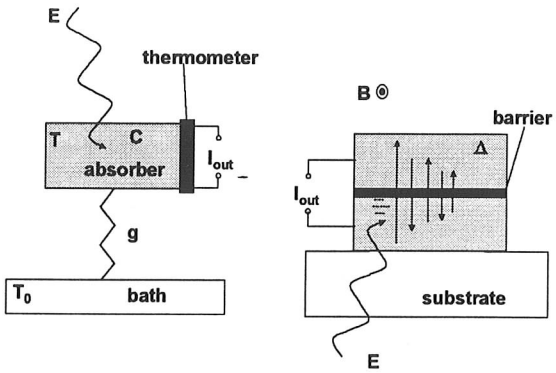

Fig. 1: A schematic of a microcalorimeter (left) and an STJ (right). The direction of illumination is indicated for both devices, as well as the magnetic field parallel to the barrier of the STJ, necessary to suppress the Josephson current..

3. Superconducting Tunnel Junctions (STJs)

A STJ consists of two superconducting layers separated by a thin insulating barrier (see Fig. 1). It requires a magnetic field parallel to the barrier to suppress the Josephson current. The operating temperature is typically ~0.1T_c, sufficiently low to avoid any significant population of thermally excited quasiparticles. The absorption of a photon with energy E in a superconductor is followed by a series of fast processes in which the photon energy is converted into free charge carriers (quasiparticles) by the breaking of Cooper pairs. For typical transition metals this conversion process ranges from nanoseconds (niobium) to microseconds (hafnium). The average number of excess carriers is $N_o(E) = E/1.7\Delta$, with Δ the energy gap of the super-conductor. Thus, in a superconductor such as tantalum (Δ=0.664 meV) the initial mean number of free charge carriers created $N_o(E)$ is ~10^3/eV. The limiting energy resolution (Fano limit) is determined by the variance on $N_o(E)$ and given by:

$$\delta E_{Fano} = 2.355[1.7\Delta EF]^{1/2}, \qquad (3)$$

where F~0.2 is the Fano factor [10,11].

The quasiparticles produced through photo-absorption can be detected by applying a d.c. potential across the thin insulating barrier of the STJ. This potential

bias favors the transfer of electrons from one film to the other through quantum mechanical tunneling across the barrier. The detector signal is therefore represented by the current developed by this tunnel process. After initial tunneling, a quasiparticle can tunnel back (see Fig.1), therefore contributing many times to the overall signal [12]. On average each quasiparticle will contribute $<n>$ times to the signal before it is lost from the system through recombination etc. Hence the mean number of *detected* charge carriers $N = <n>N_0$. The value of $<n> \sim \Gamma_{tun}/\Gamma_{loss}$, with Γ_{tun} the tunnel rate across the barrier and Γ_{loss} the loss rate in the system. Multiple tunneling can be enhanced by including layers of a lower gap material on either side of the barrier, such that quasi-particles are confined close to the barrier [13], away from possible loss sites such as surfaces. Typically $<n>$ can vary widely from 1-100 and depends on the size and nature of the STJ. Statistical fluctuations on $<n>$ will contribute to the energy resolution, resulting in the so-called tunnel-limited resolution, which, for a symmetric STJ, is given by [14,15]:

$$\delta E_{tunnel} = 2.355[1.7\Delta E\,(F+1+1/<n>)]^{1/2} \qquad (4)$$

At best ($<n> \rightarrow \infty$) $\delta E_{tunnel}/\delta E_{Fano} \sim 2.4$. The predicted tunnel-limited resolution for Ta (Δ=0.67 meV), Mo (Δ=0.139 meV), and Hf (Δ=0.02 meV) is shown in Fig. 2.

Further degradation of the energy resolution may occur due to electronic noise (δE independent of E) and detector nonuniformity ($\delta E \propto E$).

Single photon detection in the UV/visible has only been reported sofar by our group with Nb- [1] and Ta-based STJs [2]. The best results are obtained for STJs on sapphire substrates with 100 nm thick Ta base (epitaxial) and top (polycrystalline) electrodes and 5-30 nm thick Al trapping layers. The devices are read-out via charge sensitive amplifiers with JFET input stages at room temperature. Electronic noise levels of 0.1-0.2 eV are achieved for device sizes 20x20 - 100x100 μm^2, operated at T=300 mK. Pulse decay times for these devices range from 6-70 μs.

The measured energy resolution is usually best for the epitaxial base electrode, which is accessible by illumination through the transparent substrate (see Fig. 1). Our current best results are shown in Fig. 2, illustrating that the device-limited performance (obtained after subtracting electronic noise) appears to be even better than the predicted tunnel limit.

Work in other groups is in progress to achieve photon counting in the UV-optical with STJs [16,17]. A break-through in energy resolution towards the Fano-limit could be possible if the read-out noise could be significantly reduced by the use of RF Single Electron Transistors, as proposed by Schoelkopf et al. [18].

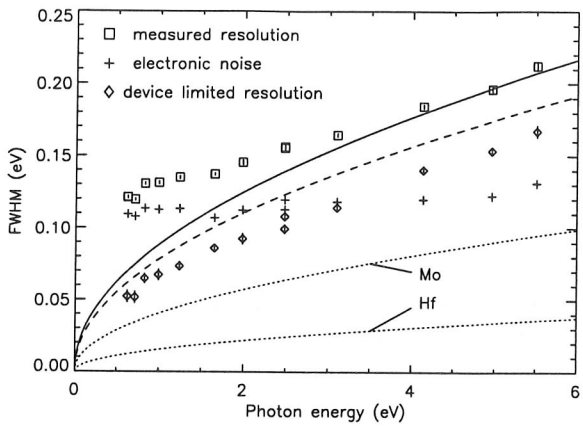

Fig. 2: Measured energy resolution for a 50x50 μm^2 Ta-based STJ, with 30 nm Al layers. The predicted tunnel-limited energy resolution is also shown for Δ=0.67 meV (for bulk Ta, solid line) and Δ=0.52 meV (as measured at the barrier of the proximised STJs, dashed line). The dotted lines represent the tunnel-limited resolution for Mo (Δ=0.139 meV) an Hf (Δ=0.02 meV).

4. Detection efficiency and IR rejection

The detection efficiency for microcalorimeters as well as STJs is primarily limited by reflection losses. For microcalorimeters this involves the surface of the absorber. For STJs in front-illumination mode it is the reflection coefficient of the top electrode metal, moderated by reflections or absorptions at insulation layers or native oxides. In the (preferred) back-illumination mode reflection at the vacuum-substrate and the substrate-metal interface and absorption in the substrate limit the efficiency. Fig. 3 shows the detection efficiency for a W-based TES and for a Ta-based STJ on sapphire in front- and back-illumination mode, calculated from optical constants [19]. In all cases, the efficiency is typically 50-70% over the UV/visible band, which is, particularly in the UV, a significant improvement over conventional detectors. The UV efficiency of the back-illuminated STJ at short wavelengths is limited by the cut-off of the sapphire substrate at λ=145 nm. This can be extended to λ=115 nm with MgF_2 as substrate material.

Work is in progress to reduce reflection losses by the use of anti-reflection coatings (STJs and TES) [20] or absorbtive 'Gold Black' coatings (TES only) [9].

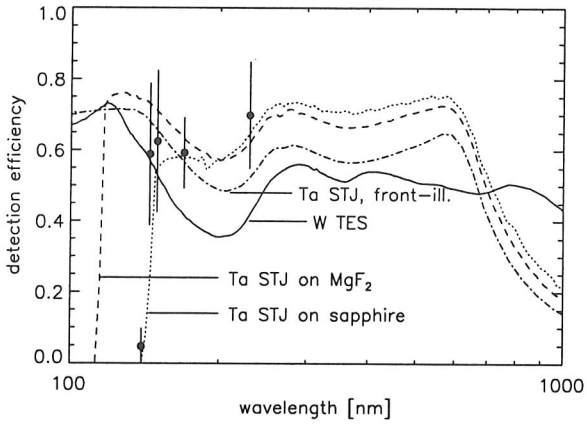

Fig. 3: Calculated detection efficiencies for a W-based TES and some configurations of Ta-based STJs. Also indicated are measured efficiencies for a back-illuminated Ta-based STJ on sapphire [2].

A serious problem is posed by the sensitivity of cryogenic detectors in the IR: the resolving power can be significantly degraded by pile-up effects of thermal IR radiation from the warm environment [21]. This requires the use of cold baffling outside the detector's field of view (FOV) and cold filters in the FOV. The problem is particularly severe compared to X-ray applications because of the lower noise levels required, and the smaller difference in wavelength, which makes the rejection of IR without loss in sensitivity difficult. The substrate of an STJ operated in back-illumination mode can already provide significant IR filtering. Some solutions, based on absorbing filters and reflecting micro-grids, are discussed in [22].

5. Imaging arrays

Astronomical applications typically require large active areas with high filling factors and good position resolution. The simplest way to achieve this with cryogenic detectors is by fabricating a close-packed array of single-element detectors, which are individually biased and read out. The problems encountered are similar for microcalorimeters and STJs: each pixel requires its own signal wire and electronics chain. This implies very dense wiring near the detector array, complex wire connecting schemes, a significant heat load on the low temperature stage and massive electronics.

Additional problems for microcalorimeters are possibly electrical cross talk and thermal cross talk via the substrate. In case of SQUID read-out, the number of wires to room temperature is at least 4-6 per SQUID. In order to reduce the wiring, a multiplexing scheme for SQUID read-out of a MxN array of detectors has been proposed and demonstrated [23]. Here, the outputs of the N SQUIDS in a column are connected in series and the bias lines of the rows are connected in parallel, thus reducing the total number of wires to room temperature to ~M+N. An 8x8 array of W TES elements with ~90% packing density is presently under development [9].

For STJs, similar issues of electrical and signal cross talk exist. In addition, high pixel uniformity is required for simultaneous suppression of the Josephson current in all pixels. The wiring problem is slightly less severe since each pixel needs only one wire for read-out and biasing, in addition to a single common return wire, contacting the interconnected base electrodes of all pixels. This concept was adopted for the 6x6 array of Ta-based STJs (25x25 μm^2) used in S-CAM [24] and demonstrated in a time-resolved observation of the Crab pulsar at the WHT telescope at La Palma, Spain [25]. Signal cross talk by diffusion of charge carriers between pixels is suppressed efficiently by making the interconnections of a higher gap material (Nb). Illumination through the sapphire substrate allows the wiring for the inner pixels to be led across the outer pixels without loss of efficiency.

A second approach – the matrix readout, connects the base film of all devices in an array from the same row and the top films from the same column [26]. A photon is then detected as a coincident event between one of the rows and one of the columns. Such an approach reduces the amount of wiring for individual devices in an MxN array and the signal processing chains to only M+N, at the expense of higher read-out noise due to the higher capacitance, and lower countrate capability.

An alternative approach to achieve larger field coverage is the use of large-area 1-D or 2-D absorbers, read out by STJs at the ends or corners of the absorbers. Charge carriers generated in the absorber after the absorption of a photon will diffuse to the STJs and give rise to tunnel currents with amplitudes depending on the position of absorption. Thus, the energy of the photon can be reconstructed from the sum of the STJ signals, whereas the position is derived from the difference. This concept, originally developed for X-ray detection [27,28], is presently being investigated in our group and at Yale University [17] for the UV-visible range. Fig. 4 shows preliminary results from our group for a 400x50 μm^2, 100 nm thick Ta absorber, including two 50x50 μm^2 Ta STJs with 65 nm thick Al trapping layers,

illuminated with 300 nm photons. The energy resolution obtained over a length of 240 μm is 0.40 eV at E=4.13 eV, with an electronic noise contribution of 0.3 eV. The estimated position resolution is <30 μm. Such absorber-STJ structures could be the basic elements of a larger format array, albeit with reduced count rate capability.

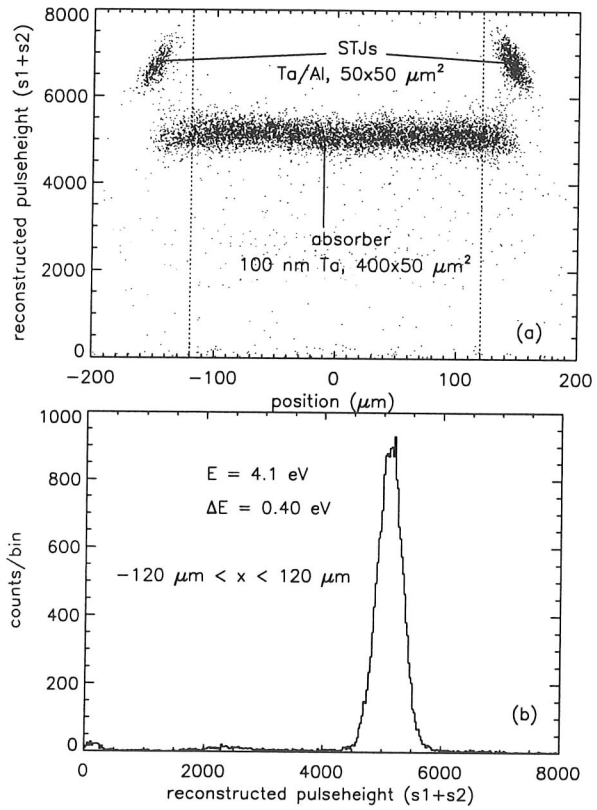

Fig. 4: (a) reconstructed pulse height (s1+s2, corrected for position-dependent losses) vs position (∝(s1-s2)/(s1+s2)) on the absorber for E=4.1 eV photons (b) pulse height spectrum for the region −120 μm < x < 120 μm.

6. Conclusion

The presently available cryogenic detectors in the UV/optical (Ta-based STJs and microcalorimeters with W-based TES) achieve detection efficiencies of 50-70% and an energy resolution δE ~0.15 eV at E=3 eV. Further improvements in resolution should be possible if lower T_c materials are used. With fast pulse decay times of order ~10 μs, they should be able to detect up to ~10^4 cts/s. The fast photometric capabilities of both detector types have been demonstrated by measurement of the Crab pulsar light curve. Small imaging arrays (<100 pixels) based on individual read-out of pixels have been demonstrated for STJs and are being developed for micro-calorimeters. The main challenge is now to expand these arrays to larger formats (>1000 pixels), which requires the development of sophisticated read-out schemes.

Acknowledgements

The author gratefully acknowledges the work of the ESTEC detector development group, the Oxford Instruments Scientific Research Division, Cambridge, UK and Cambridge Microfab Ltd., Cambridge, UK.

References

[1] A. Peacock et al., Nature 381 (1996) 135.
[2] P. Verhoeve et al., Proc. of LTD7, Munich 1997, ISBN 3-00-002266-X, p97.
[3] B. Cabrera et al. Appl. Phys. Lett. 73 (1998) 735.
[4] T. Peacock et al., Astron. and Astrophys. Suppl. Ser. 127 (1998) 497.
[5] P. Jakobsen, ASP Conf. Series 164 (1999) 397.
[6] J.M. Shull et al., Report of NASA UV-optical Working group, http://xxx.lanl.gov/archive/astro-ph.
[7] K.D. Irwin, Appl. Phys. Lett. 66 (1995) 1998.
[8] K.D. Irwin, G.C. Hilton, D.A. Wollman, J. M. Martinis, Appl. Phys. Lett. 83 (1998) 3978.
[9] A.J. Miller et al., to be published in SPIE proceedings 3764, (1999).
[10] M. Kurakado, Nucl. Instr. and Meth. 196 (1982) 275.
[11] N. Rando et al., Nucl. Instr. and Meth. A313 (1992) 173.
[12] K.E. Gray, Appl. Phys. Lett. 32 (1978) 392.
[13] N.E. Booth, Appl. Phys. Lett, 50 (1987) 293.
[14] C.A. Mears, S.E. Labov and A.T. Barfknecht, Appl. Phys. Lett. 63 (1993) 2961.
[15] D.J. Goldie et al., Appl. Phys. Lett. 64 (1994) 3169.
[16] B. Delaet et al., these proceedings.
[17] C. Wilson, these proceedings.
[18] R.J. Schoelkopf et al., IEEE Trans. on Appl. Supercon. 9 (1999) 2935.
[19] E.D. Palik, ed., Handbook of optical constants of solids, Academic Press Inc, 1985.
[20] M. Rajteri, these proceedings.
[21] J.B. Legrand et al., Proc. of LTD7, Munich 1997, ISBN 3-00-002266-X, p106.
[22] N. Rando, P. Verhoeve et al., these proceedings.
[23] J.A. Chervenak et al., Appl. Phys. Lett. 74 (1999) 4043.
[24] N. Rando, et al., SPIE Proc. 3435 (1998), 74.
[25] M.A.C. Perryman, F. Favata, A. Peacock, N. Rando, B.G. Taylor, Astron. and Astrophys. 346 (1999) L30.
[26] D.D.E. Martin et al., submitted to J. Appl. Phys., 1999.
[27] H. Kraus et al., Physics Lett. B 231 (1989) 195.
[28] K. Segall et al., IEEE Trans. on Appl. Supercon. 9 (1999) 3326.

IR Filters for High Responsivity Cryogenic Detectors

N. Rando[1], P. Verhoeve[1], P. Gondoin[1], B. Collaudin[2], J. Verveer[1], M. Bavdaz[1], A. Peacock[1]

[1]ESA/ESTEC, Astrophysics Division, P.O.Box 299, Space Science Department, 2200 AG Noordwijk, The Netherlands
[2]ESA/ESTEC, Thermal Control and Life Support Division, Mechanical Systems Department, P.O.BOX 299, 2200 AG Noordwijk, The Netherlands

ESLAB 1999/063/SA

To be published in Proceedings of the 8th International Workshop on Low Temperature Detectors
Dalfsen – The Netherlands, 15-20 August 1999

IR filters for High Responsivity Cryogenic Detectors.

8th International Workshop on Low Temperature Detectors

N.Rando, P.Verhoeve, P.Gondoin, B.Collaudin[(1)], J.Verveer, M.Bavdaz, and A.Peacock.

Astrophysics Division, Space Science Department,
[(1)] Thermal Control and Life Support Division, Mechanical Systems Department,
European Space Agency, ESTEC, Noordwijk, The Netherlands.

Abstract

Modern cryogenic detectors, such as Superconducting Tunnel Junctions and Transition Edge Sensors, provide single photon counting performance, medium to high energy resolution, high count rates and good photon collection efficiency over a wide wavelength range. In order to avoid background limited performance, it is necessary to shield the detectors from any thermal IR radiation originating from the surrounding warm surfaces. In this paper we analyse the contribution of the thermal radiation to the detector performance and describe the IR filters used in the *S-Cam* camera and in other experimental configurations. Future detectors may require very severe attenuation of the IR flux (λ>1 μm). Solutions to this problem are proposed and their validity demonstrated with experimental results.

Keywords: electro-optical instrumentation, cryogenic detectors, IR filters.

1. Introduction

Modern cryogenic photon detectors provide single photon counting performance from NIR to X-ray energies [1, 2]. In the case of a tantalum based STJ, responsivities are of order 10^4 *e-/eV*, resolving power E/ΔE is of order 20 at λ = 300 *nm* and quantum efficiency is about 70% in the visible range. Typical operating temperatures are about 300 *mK* for Ta and Nb-Al based STJs and of order 100 *mK* for Transition Edge Sensors (TES). In order to avoid background limited performance, it is necessary to reject any thermal radiation from warmer elements in the Field Of View (FOV) of the detectors. Such an issue is particularly challenging in the case of instruments targeting the lower photon energy range (e.g. visible range). While soft X-ray and UV applications can take advantage of very thin Al filters [3], instruments operating in the visible range must provide high IR rejection combined with an adequate optical throughput. As predicted by the Planck distribution, the number of photons emitted by a grey-body is very large when compared to the low count rates expected from typical signal sources (e.g. faint astronomical objects). This is the case of *S-Cam*, an astronomical camera for ground-based astronomy in the visible range, recently installed at the Nasmyth focus of the William Herschel Telescope, in La Palma, Canary Islands (Spain) [4,5]. The effects of IR radiation applied to the cryogenic detectors are of two-fold nature: 1) they may represent a heat load, increasing the detector temperature; 2) they produce a large number of photo-absorptions in the detector, thus generating pile-up effects and a corresponding degradation of the intrinsic energy resolution [6].

In the case of a linear detector, with responsivity *R*, the signal *S* measured over an integration time τ_i is $S = R \cdot E$, with *E* the energy of the detected photon. The effects of an infrared photon absorption rate Γ_{IR} are: 1) the continuous absorption of IR photons determines an increase of the detector noise, σ_{DC}; 2) fluctuations in the total amount of energy absorbed within the integration time produce an additional variance on the detector signal, σ_{IR}. In the case of a superconducting tunnel junction (*e* = electron charge) we can write that [6]:

$$\sigma_{DC}[e^-] = \sqrt{e \cdot R \cdot < E_{IR} > \cdot \tau_i \cdot \Gamma_{IR}} \quad (1)$$

$$\sigma_{IR}[e^-] = R \cdot \sqrt{< E^2 > \cdot \tau_i \cdot \Gamma_{IR}} \quad (2)$$

σ_{DC} and σ_{IR} are expressed in electrons and represent the additional variance on the detector signal induced by the presence of thermal background radiation. It can be shown that $\sigma_{IR} > \sigma_{DC}$ if $<E_{IR}> > e/R$, condition which is generally met. In the case of *S-Cam* (*R* = 6000

e-/eV) the condition above is met for any thermal IR radiation emitted by grey bodies at temperatures larger than a few degree Kelvin. Large IR photon fluxes can induce a local heating of the detector substrate, thus influencing its performance. This effect is important for STJs, whose bias current is strongly dependent on temperature: to small temperature increases may correspond a large change in the shot noise over a given frequency bandwidth Δf, as from equations (3) and (4):

$$I_{sg}(\Delta,V,T) = I_0(V,\Delta)\cdot\sqrt{2\pi\cdot k\cdot T\cdot\Delta}\cdot e^{-\Delta/kT} \quad (3)$$

$$\sigma_{th}[e^-] = \sqrt{2\cdot e\cdot I_{sg}(\Delta,V,T)\cdot\Delta f} \quad (4)$$

In a tantalum STJ, a temperature variation from 400 *mK* to 500 *mK* quadruples the current, thus doubling the shot noise [7]. In the case of sapphire substrates, a heat input of order 1 μW due to IR radiation is enough to increase the detector temperature by more than 100 *mK*. It is evident how the noise increase related to heating effects can be as important as the energy degradation described by eq. (1) and (2).

2. IR filter solutions

In order to attenuate the effects of the IR radiation two approaches are followed: 1) use of severe baffling, strictly limiting the detector field of view (FOV) to the application needs; 2) adoption of filtering elements. A combination of the two techniques is often required. In the case of filters, in addition to the band-pass, we must take into account their own grey-body thermal emission: thus, it is necessary to maintain the filtering elements at cryogenic temperature.

Different filtering configurations have been investigated by illuminating a Ta STJ detector (kept at 450 mK) through the sapphire substrate. In each case the filtering element was clamped to the 4K shield of the cryostat. The filter attenuation factor is proportional to the ratio of the sub-gap current densities Jsg (at 100 μV), measured with and without the filter. The measured attenuation was compared with calculated values, under the assumption of 300K black-body radiation reaching the detector through the filters. The comparison showed that the measured attenuation was lower than predicted on the basis of the estimated IR flux (eq. 1 and 2). This suggested that heating of the substrate is likely to be present, enhancing the effect of the IR background (see eq. 3 and 4). In addition to sapphire and quartz, we have also tested a 100 nm thick Al filter, opaque to visible light, and a conductive micro-grid, a diffraction based IR blocking filter. The main results are summarised in the table below.

Configuration:	Jsg attenuation.
No filter	1
Sapphire (at 4 K)	0.12
Micro-grid on sapphire (at 4K)	0.0069
SiO2 (at 4 K)	0.0034
Thin Al filter (at 4 K)	0.0017

The thin Al filters represent an ideal solution for soft X-ray applications, ensuring adequate transmittance to higher energy photons (typ. above 50% at 60 eV) and being opaque to visible and IR radiation (transmittance of order 10^{-8}). In our case the filter was procured from Luxel (US): it is made of an Al:Si foil 101 nm thick, and supported by a Ni mesh [3]. A Cu flange allows the installation on the thermal shield of the cryostat. The micro-grid (figure 1) was fabricated by IMM (D), by etching a WSi layer deposited on a sapphire substrate. The grid is 500 nm thick and has hexagonal shape, with an estimated open/masked area ratio of 50% and an average hole size of about 480 nm.

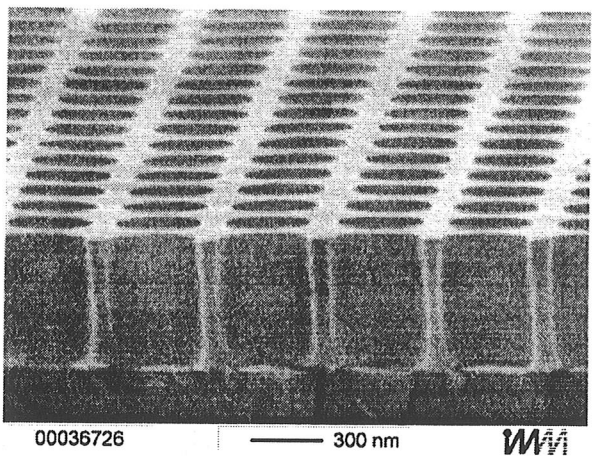

Figure 1: metallic micro-grid on sapphire (IMM-D).

Such metallic meshes have frequency selective properties: wavelengths shorter than the mesh hole size pass through, while longer wavelengths are severely reflected out [8].

3. The S-Cam configuration

S-Cam is a cryogenic camera based on a 6x6 array of Ta-Al-AlOx-Al-Ta STJs [4]. It has been designed to operate at the Nasmyth focus of the *William Herschel Telescope*. A demagnification unit is required to

achieve the desired plate scale on the camera focal plane (0.6 arcsec/pixel). Such a unit has an exit focal ratio f=2.06 (i.e. an opening angle θ = arcsin (1/2f) = 14.05 degree) and a back focal length d=68 *mm*. At this distance, the area of the cryostat window in the FOV of the detector is $A = \pi \cdot [d \cdot \tan(\arcsin(1/2f))]^2$ = 910 mm^2. The thermal radiation originated from this surface at T=293 K corresponds to a heat input Q_{in}. Under the assumption of an inner surface at a temperature T_{in} = 2 K (<< 293 K), with an effective emissivity $\varepsilon^* \approx 0.5$, we can estimate $Q_{in} = A \cdot \varepsilon^* \cdot \sigma \cdot T^4 \approx$ 200 *mW*, representing a major heat input source for our cryogenic system and a correspondingly large IR load for our detector. In order to minimise such an IR load, we have used two different filters, both located inside the cryostat and in good thermal contact with the cold plate (at about 2 K). Both elements are based on Schott KG2 coloured glass, which is well known for its IR rejecting qualities. The first filter (IRF_1) is 9 mm thick and has a diameter of 36 mm; it is mounted onto a dedicated copper holder. The second filter (IRF_2) is located inside the former of the SC magnet required to operate the detector array and also connected to the cryostat cold plate. Figure 2 shows the combined transmissivity of the two filters.

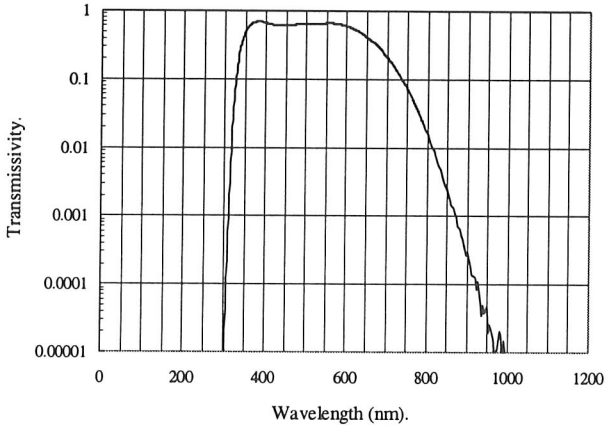

Figure 2: combined transmissivity of the two KG2 elements, IRF_1 and IRF_2.

The first filter is the most critical element, being subject to the intense radiation load produced by the window and by the warm part of the cryostat baffle. Dedicated measurements have shown that the inner surface of such a filter reaches a temperature of about 12 K. The second filter is 3 mm thick and provides additional IR attenuation, absorbing the residual IR radiation transmitted and emitted by IRF_1. Due to the much lower thermal flux, the inner temperature of IRF_2 coincides with the cold plate temperature. The cold absorbing elements modify the spectrum of the thermal radiation originally produced by the cryostat window, with the emission of longer wavelength photons. Experimental tests based on this filtering configuration have demonstrated a resolving power $\lambda/\Delta\lambda$ of order 5 at λ=500 nm, a factor 1.3 worse than the best experimental results obtained with the same detector and Front-End, but in absence of any significant IR radiation. Such a result proves that the camera is still operating in background limited conditions.
It should be noted that the intrinsic detector resolving power (in absence of any electronics and IR induced noise) at this wavelength corresponds to about 17 [9].

4. Conclusions

The suppression of any residual thermal IR radiation is a key issue for the full exploitation of the potential of modern cryogenic detectors. Thin Al filters provide an excellent solution at UV and X-ray wavelengths, while applications in the visible are more problematic.
The IR filtering solution adopted in S-Cam, while achieving single photon counting in the visible range does not allow to fully exploit the intrinsic energy resolution of the detector array. Alternative solutions, such as metallic meshes and different absorbing glasses, are being investigated to overcome such limitations.

References

[1] B.Cabrera et al. Appl.Phys.Lett. 73, 735 (1998).
[2] A.Peacock et al. Nature, 381, 135 (1996).
[3] F.R.Powell et al. Opt.Eng., 29, 614-624 (1990).
[4] N.Rando et al. Proc. of SPIE 1998, vol.3435.
[5] M.Perryman et al. Astron. Astrophys. 346, L30-L32 (1999).
[6] J.B.le Grand et al. 106-107, Proc. of LTD-7, Munich (1997), ISBN 3-00-002266-X.
[7] N.Rando et al. J.Appl.Phys. 77, 4099 (1995).
[8] Shung-Wu Lee et al. IEEE Trans. Antenna Propagat. Vol. AP-30, 904-909 (1982).
[9] P.Verhoeve et al. IEEE Trans.Appl.Supercon. 7, 3359 (1997).

First Astronomical Results from *S-Cam*

N. Rando[1], S. Andersson[1], B. Collaudin[2], F. Favata[1], P. Gondoin[1], A. Peacock[1]
M. Perryman[1], J. Verveer[1], D.J. Goldie[3]

[1]*ESA/ESTEC, Astrophysics Division, P.O.Box 299, Space Science Department, 2200 AG Noordwijk, The Netherlands*
[2]*ESA/ESTEC, Thermal Control and Life Support Division, Mechanical Systems Department, P.O.BOX 299, 2200 AG Noordwijk, The Netherlands*
[3]*Oxford Instruments, Scientific Research Division, Newton House, Cowley Road, Cambridge Business Park, United Kingdom*

ESLAB 1999/037/SA

To be published in Proceedings of the 8th International Workshop on Low Temperature Detectors
Dalfsen – The Netherlands, 15-20 August 1999

First astronomical results from *S-Cam*.

8th International Workshop on Low Temperature Detectors

N.Rando, S.Andersson, B.Collaudin[1], F.Favata, P.Gondoin, A.Peacock, M.Perryman, J.Verveer, P.Verhoeve and D.J.Goldie[2].

Astrophysics Division, Space Science Department,
[1] Thermal Control and Life Support Division, Mechanical Systems Department,
European Space Agency, ESTEC, Noordwijk, The Netherlands.
[2] Scientific Research Division, Oxford Instruments, Cambridge (UK).

Abstract

S-Cam is a cryogenic camera for ground based astronomy based on a 6x6 array of Superconducting Tunnel Junctions (STJs). The camera has been designed as a technology demonstrator, aiming to prove the potential of this new generation of single photon counting detectors at a ground-based telescope. In this article we provide an overview of the detector performance, a description of the *S-Cam* system and a summary of the test results. The first astronomical data obtained at the *William Herschel Telescope* (WHT) in La Palma (Canary Islands, Spain) are also described.

Keywords: electro-optical instrumentation, cryogenic detectors, astronomy.

1. Introduction

High quality Ta-Al based Superconducting Tunnel Junctions (STJs) can be used as single photon counting detectors in a broad energy range, from the Near Infrared to the UV and soft X-ray [1, 2]. Such a broad energy range is combined with large responsivity (of order 10^4 *e-/eV*), high quantum efficiency (in excess of 50% at visible wavelengths), adequate energy resolution ($\lambda/\Delta\lambda$ of order 10 at 300 *nm*) and fast response time (of order 10 μs). The fast response time allows for high count-rates and for the capability to associate a well-defined time of arrival to each detected event. Most importantly, such a device is the first optical detector which can determine, intrinsically (without the use of dispersive elements or filters), the energy of each individual photon [2], thus allowing the construction of imaging spectrometers.

2. The S-Cam array

A detailed description of the photo-absorption process taking place in STJ based detectors has been given elsewhere [1,2]. The excess charge produced by the photo-absorption is detected as a current pulse, driven by a dc voltage bias applied across the tunnel barrier, between the two electrodes forming the STJ. The intrinsic energy resolution of an STJ detector is limited by statistical fluctuations in the charge originally produced in the superconducting absorber (related to the Fano factor, $F \cong 0.22$) and in the average number of tunnels <n>. In the case of a symmetrical junction, the intrinsic detector resolution (Full Width at Half-Maximum, FWHM) can be written as [1]:

$$\Delta E_d(eV) = 2.355 \cdot \sqrt{\varepsilon \cdot E \cdot (1 + F + 1/\langle n \rangle)} \qquad (1).$$

For a Ta based detector, with $\langle n \rangle \rightarrow \infty$, the limiting energy resolution corresponds to about 0.14 *eV* at 2.48 *eV* (λ=500 *nm*), with an intrinsic resolving power $E/\Delta E = \lambda/\Delta\lambda \cong 18$. The total energy resolution is degraded further by electrical noise and by pile-up effects induced by the presence of any IR background radiation [3]. In order to optimise the detector performance it is therefore necessary to minimise the IR background by using an adequate filtering configuration.

The *S-Cam* array (figure 1) is based on 36 diamond-shaped, 25 μm devices. The detectors are fabricated from an original Ta-Al-AlOx-Al-Ta multilayer, deposited by sputtering and within a single UHV run onto a sapphire substrate. The 100 *nm* thick, epitaxial Ta base electrode is deposited first (with a Residual Resistance Ratio of order 45), followed by 5 *nm* of Al. After the barrier oxidation process, further 5 *nm* of Al

are sputtered, together with the top film of 100 *nm* thick Ta. A 350 *nm* thick SiOx passivation layer is then deposited onto the multilayer. The junctions have a barrier resistivity of order $3 \cdot 10^{-6} \Omega \cdot cm^2$, with leakage limited subgap current densities of order 0.1 $pA/\mu m^2$ at a bias voltage of 0.1 *mV* and at T=300 m*K*. The device energy gap, deduced from the I-V characteristics, is 0.665 *meV*.

The *S-Cam* array geometry has been optimised [4] to reduce simultaneously the dc Josephson current below 50 *nA* for each of the 36 pixels at a field intensity of about 100 *G*. The electrical connections to the counter-electrode of the single devices are in Nb, deposited onto the SiOx passivation layer and connecting each pixel through small vias opened in the isolation layer. The detection of visible photons takes place in the base electrode of the device, through the sapphire substrate. The quantum efficiency of the single detector in back-illumination is in excess of 70% from 200 to 800 *nm* [5]. The active area of the detector, with 4 μm gaps separating the pixels, corresponds to 74.3 % of the total array area. The base electrodes of the pixels are connected via small Nb bridges to minimise the diffusion of quasiparticles from one pixel to the adjacent ones [6]. Dedicated time coincident tests have shown that the cross talk by diffusion from one pixel to the neighbours is about 8 % [7].

Tests have also confirmed that it is possible to operate simultaneously all pixels at a bias voltage of about 150 μV, with uniform responsivity ($R \cong 60 \cdot 10^3$ *e-/eV*). The detectors have a characteristic pulse decay time of about 7 μs.

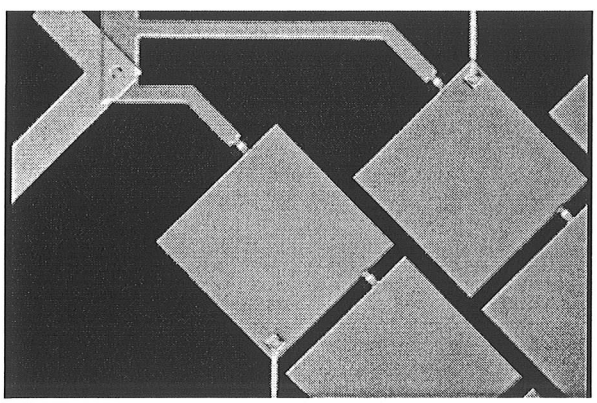

Figure 1: detail of the 6x6 Ta-Al based S-Cam array. The Nb bridges connecting the base electrodes of adjacent pixels are clearly visible.

3. S-Cam design and performance

The development of *S-Cam* is based on the instrument requirements listed in the table below and reflecting both the operational needs and the observation site characteristics [8]. The system is designed to operate at the Nasmyth focus of the William Herschel Telescope. A plate scale of 0.6 *arcsec/pixel* was selected to match the telescope seeing (typically slightly below 1 *arcsec*). The camera is composed of an optical unit, a cryogenic system based on a ^{4}He cryostat and hosting a ^{3}He cryo-sorption cooler, analog front-end electronics and digital data acquisition and storage equipment. The optical unit and the cryostat are located on an optical bench inside the GHRIL (Ground-based High-Resolution Imaging Laboratory) room, a dark cabin which is at one of the two Nasmyth foci of the alt-azimuth telescope.

Nominal band-pass:	350 - 650 *nm*.
Provided data / event:	λ, arrival time, pix. address
Resolut. (λ/Δλ(fwhm)):	of order 4 at 500 *nm*.
Event time accuracy:	5 μsec (UTC).
Max. count rate/ pixel:	1 *Khz*.
Camera field of view:	4.0 x 4.0 $arcsec^2$.
Plate scale:	0.6 *arcsec/pixel*.
Data storage format:	FITS format

A filter wheel unit allows to use neutral density and pass band filters. A superconducting magnet provides the field required to suppress the Josephson current and bias the detector. The STJ's are read-out by 36 room temperature Charge Sensitive Preamplifiers. The total detector noise is about 1200 *e-* rms (corresponding to about 0.5 *eV*, FWHM). The time tagging information is provided by a time reference receiver based on the Global Positioning System. Such a time reference is within 1 μs of UTC. The control of the instrument is performed from the telescope control room, via a PC. The data are stored in the FITS (Flexible Image Transport System) format.

The observed degradation of the energy resolution (from λ/Δλ=17 to 4 at 500 nm) is due to pile-up effects induced by the thermal radiation and to electrical noise. In order to reject the IR radiation, *S-Cam* uses two KG2 glass filters of different thickness, cooled at a temperature of 12 and 2 K respectively. The instrument resolving power (λ/Δλ) is typically of order 4 at 500 nm and constant from pixel to pixel within 10%. The total camera throughput in the nominal band-pass is of order 30 %. The cryogenic system provides a base temperature of 320 mK and a hold time in excess of 8 hours.

4. Astronomical results

S-Cam was shipped at the beginning of January 1999 to the WHT, the largest telescope in Europe. It has a classical Cassegrain configuration and a paraboloidal primary mirror with a 4.2 *m* diameter. Astronomical observations concentrated on time varying objects, in order to take advantage from the time-tagging performance of the camera. The Crab pulsar, PSR 0531+21, in the Crab Nebula, provides an excellent target for the verification of the astronomical performance of a time-resolved instrument [9] and it remains one of the few pulsars observed to emit pulsed optical radiation. Our observations took place on 4-6 February, in modest seeing conditions (> 2 arcsec). Photon arrival times have been translated to the solar system barycentre, taking into account the propagation delay. Figure 2 shows the light curve from a 50 min observation (Feb 6) over the range 310-610 nm, with 128 phase bins (corresponding to about 250 μs per bin). The two peaks correspond to the emission from the two different magnetic poles of the spinning neutron star. The measured period is consistent with the literature radio values within 5 x 10^{-8} sec. Further analysis has been conducted by splitting the data in two energy bins, E1=310-410 nm and E2=500-610 nm. Within the modest energy resolving power of the instrument, no significant colour index variations with the pulsar phase exist. Additional details can be found in [10].

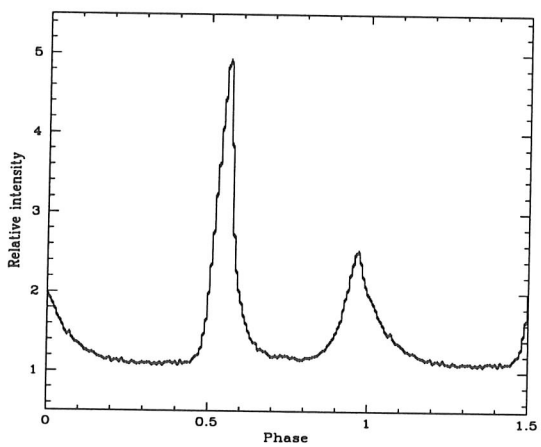

Figure 2: Pulse profile for the Crab pulsar from the 6 Feb 1999 data (310-610 nm range, 50 min observation).

5. Conclusions

The simultaneous imaging, time resolution and spectro-photometric capabilities make STJs a good candidate for the next generation of detectors for optical astronomy. *S-Cam* has been developed as a technology demonstrator capable of producing astronomically relevant data. In this prototype the scientific applications are limited by the small FOV and by the modest spectral resolution. Nevertheless, the good time resolution has allowed spectro-photometric studies of time variable objects, such as the Crab pulsar.

An improved version of our camera is being developed, including a larger field of view, higher count-rate capability, enhanced resolving power and simplified operations. A new observation campaign is scheduled for the end of 1999.

Possible applications of this technology outside astrophysics involve materials science diagnostics, biomedical instrumentation and remote sensing, with particular regard to high-speed spectro-photometry, low light level spectroscopy and the study of luminescence phenomena.

References

[1] T.Peacock et al. Astron. Astrophys. Suppl. Ser. 123, 581-587 (1997).
[2] A.Peacock et al. Nature, 381, 135 (1996).
[3] J.B.le Grand et al. 106-107, Proc. of LTD-7, Munich (1997), ISBN 3-00-002266-X.
[4] R.L.Peterson, Cryogenics, 31, 132 (1991).
[5] P.Verhoeve et al.IEEE Trans.Appl.Supercon., 7, 3359 (1997).
[6] N.E.Booth, Appl.Phys.Lett. 50, 293 (1987).
[7] N.Rando et al. Proc. of SPIE 1998, vol.3445.
[8] N.Rando et al. Proc. of SPIE 1998, vol.3435.
[9] R.W.Romani et al. Ap.J., 521, L153-156 (1999).
[10] M.Perryman et al. Astron. Astrophys. 346, L30-L32 (1999).

Acknowledgements

We would like to acknowledge the key role played by Bent Christensen (Unigate Technologies, DK) in the development of the complete camera software. R.Hart and D.Glowacka (Oxford Instruments, UK) have provided invaluable support during the detector manufacturing. Finally, we acknowledge the excellent support from the WHT staff and in particular P.Moore and C.Benn (Isaac Newton Group, La Palma, Spain).

New Readout Scheme for Superconducting Tunnel Junction Arrays

A. Peacock[1], P. Verhoeve[1], A Ploelaert[1], R. Venn[2]

[1]*ESA/ESTEC, Astrophysics Division, P.O.Box 299, Space Science Department, 2200 AG Noordwijk, The Netherlands*
[2]*Cambridge MicroFab Ltd., Trollheim Cranes Lane, Kingston, Cambridge CB3 7NJ, United Kingdom*

ESLAB 1999/067/SA

To be published in Proceedings of the 8th International Workshop on Low Temperature Detectors
Dalfsen – The Netherlands, 15-20 August 1999

New Readout Scheme for Superconducting Tunnel Junction Arrays

D. D. E. Martin[a], A. Peacock[a], P. Verhoeve[a], A. Poelaert[a], R. Venn[b]

[a]*Astrophysics Division, Space Science Department of the European Space Agency, ESTEC, Keplerlaan 1, 2201 AZ Noordwijk, The Netherlands*
[b]*Cambridge MicroFab Ltd., Trollheim Cranes Lane, Kingston, Cambridge CB3 7NJ, UK*

Abstract

We report on the design and testing of a new readout scheme for Superconducting Tunnel Junction (STJ) arrays. This method drastically reduces the number of connections and electronic circuits required for reading out an array of pixelated detectors. In the specific case of STJs, it eases the manufacturing process and connectivity problems. It is a generic scheme in that it could also be applied to different kinds of detector arrays. The experiments reported are simply a proof of principle and were carried out on a two-by-two array of STJs using optical photon excitation on Tantalum based detectors. If one uses charge sensitive amplifiers with junction field-effect transistors (JFETs) we verify that the resolution degrades mainly due to capacitance increase at the input node. However, since each detector is read-out by two independent circuits, these two outputs can be combined to increase the signal-to-noise level. We show that the equivalent noise charge at the input worsens by about a factor <N as compared to individual read-out and for a NxN array, consistent with our theoretical predictions. If one uses Superconducting Quantum Interference Devices (SQUIDs) as pre-amplifying stage, there should be no considerable increase in electronic noise related to this new readout scheme.

1 Introduction

During the last few years, non-dispersive detectors based on superconducting materials such as Superconducting Tunnel Junctions (STJs) or Transition Edge Sensors (TESs) have been developed to such an extent that they have now demonstrated rather high energy resolutions. Reported values range from 0.12-0.3eV full width at half maximum (FWHM) in the optical wavelengths using STJs [1,2] to 7eV (FWHM) at 6keV X-ray energies using a TES [3]. The next step in the development of these detectors is to group them into arrays so as to obtain an imaging capability.

These cryogenic detectors have all been read out using individual acquisition chains for each pixel. This severely limits the number of pixels for three main reasons:

i. All these detectors require very low operating temperatures (0.1-0.3K) and the most serious problem is related to heat load onto the cryogenic cooler through the wiring between the room-temperature electronics and the detector.

ii. The second problem concerns more the specific case of the application to space instruments where power consumption and weight are to be minimised. Indeed, each pixel requires an individual readout chain comprising a biasing circuit and a preamplifier, shaping filter, low-level threshold detector, sample-and-hold and analog-to-digital converter circuits.

iii. In the specific case of front illumination by soft X-rays, the amount of wiring crossing the detectors effectively kills the low energy response.

We describe here a potential new method for reading out large format arrays of pixel detectors which dramatically reduces the number of wires on chip as well as the number required between the detector and the acquisition electronics and reduces by the same amount the number of electronic channels. With this new method, which we shall refer to as matrix read-out, an array of NxN pixels can be read-out by 2xN amplifier chains instead of the normally required N^2.

The discussions and illustrations will be based on STJ arrays but we believe the concept is more generic, being applicable to a wider range of detectors (e.g. TES arrays).

2 The Pixel Array Interconnection Principle

2.1 Introduction

The principle is based on interconnecting the pixels in rows and columns as shown in figure 1. In this specific case of an STJ array, the base electrodes are interconnected in rows and the top electrodes in columns. Each row and each column is connected to a separate bias and amplification circuit. This means only 2xN wires and circuits are needed to read out a NxN array, instead of the traditional N^2.

When a pixel has been hit by a photon, the excess tunnel current will produce a signal proportional to the photon's energy simultaneously in its corresponding row and column.

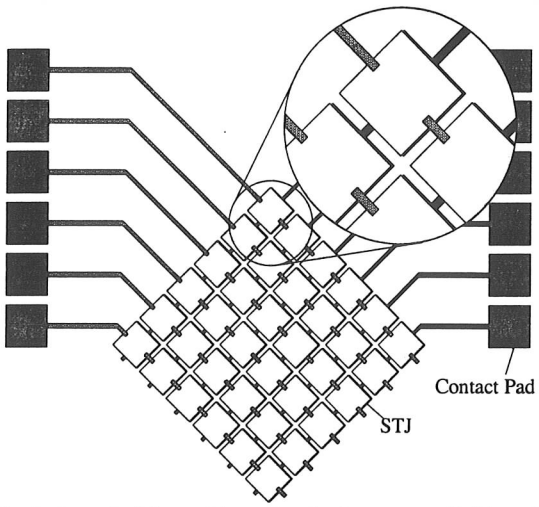

Fig. 1. Layout of the matrix read-out scheme as applied to a 6x6 STJ array. Grey tracks are connected to the top electrodes; black tracks are connections to the base electrodes.

A coincidence measurement between rows and columns can therefore determine which pixel recorded the photon event. The photon's energy can be derived, as usual, by filtering the integrated charge output from the charge sensitive preamplifier using a pulse shaper followed by a peak detector.

Obviously, with the proposed readout approach, the number of wires and circuits for reading out a large format array can be reduced dramatically. A conventional approach would currently limit the number of pixels to about 100 and with major development (particularly related to the cryogenic cabling) possibly to 10^3 due to excessive heat load on the cryogenic system. We can now however envisage arrays of 10^4 to 10^6 pixels. Such large format arrays open up the possibility to develop large format, large field-of-view imaging spectrometers for UV-optical astronomy and high-energy X-ray astrophysics.

This scheme does not require additional processing steps in the fabrication of the array chips. Since it avoids tracks covering the top electrode, this method also eliminates their masking, especially troublesome for low energy X-ray detection.

2.2 *Possible Drawbacks with the Readout Approach*

2.2.1. Electronic noise considerations

If we consider a single STJ connected to a JFET charge-sensitive pre-amplifier, the major noise sources are the JFET's series noise and the parallel noise consisting of the detector bias current's shot noise and Johnson noise from the feedback resistor [4,5].

The parallel noise power density due to the detectors' leakage currents will increase by a factor N compared to the single detector case, but should remain negligible with high quality barriers.

The proposed read-out scheme affects in two ways the output noise related to the JFET's input referred (series) voltage noise. Firstly, this component is directly influenced by the input node capacitance, which increases by a factor N as perceived at the output of a NxN detector array. Indeed, in the new read-out scheme, each amplifier senses a parallel combination of N detectors. Secondly, each row (column) is connected to each column (row) amplifier through the detectors. The series noise related to the column (row) amplifiers are therefore also coupled in through the detectors' capacitance [6]. Since each photon event is recorded in its row and column and since the corresponding noise source are mainly uncorrelated, both signals can be combined to increase the signal-to-noise ratio. It can be shown [6] that in the case of series noise limited electronics, the noise factor increase for the matrix readout compared to the individual readout scheme is $< (N+\sqrt{N})/\sqrt{2}$.

If the preamplifier's first stage is a SQUID, this factor can be eliminated because of the absence of series noise [4].

2.2.2. Count rate issue

A photon absorbed in a particular junction has to be localised by a simultaneous detection in the corresponding row and column. If another photon is absorbed in another junction within the electronic response time, position ambiguity and possible pile-up can result. The position ambiguity can be resolved by using a fast threshold detection circuit. In principle, sub-microsecond response times are possible since a slow shaping time (optimised for best signal-to-noise ratio) is not required for detection purposes. Therefore >1MHz rates are theoretically feasible. Pile-up will occur if two events are absorbed either in the same junction or in the same row or column. Pile-up within the same junction is, of course, identical to the individual read-out case.

2.2.3. Diagnostics and yield

STJs are normally diagnosed by tracing their current versus voltage (IV) characteristic. Due to the fact that all junctions are interconnected in the matrix scheme, it becomes impossible to diagnose individual detectors. However, an IV curve is still a good analysis tool in that it will provide upper limits to the Josephson and sub-gap currents of the devices.

Note however that if a junction has a short, cannot be biased or is too noisy, it will spoil the complete row and column. This could pose a serious yield problem for large arrays.

3 Test Results

The chip used for this test was a Tantalum based 6x6 array. At the time of the tests, only a 4-channel electronics system was available which limited us to a subset of 2x2 detectors. The selected junctions were connected to the 4 individual electronic channels as shown in Figure 2. In order to detect photons, each pre-amplifier channel is followed by a slow and a fast shaping filter. The fast filter is used

for triggering and time stamping the events while the slow filter is optimised for accurate pulse amplitude measurements. Data files contain an event list of the fast and slow samples of all 4 channels and a time stamp for each trigger. A Xenon lamp with a programmable double monochromator was used as a light source and coupled to the detector array via an optical fibre. Illumination was through the sapphire substrate.

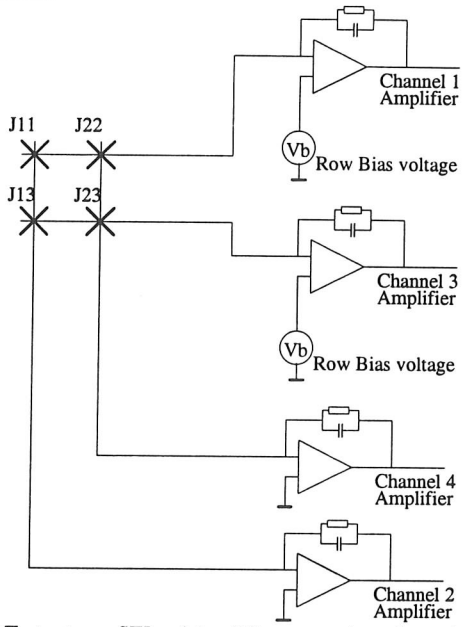

Fig. 2. Test set-up - STJ and Amplifier connection schematic

3.1 *Channel Correlation*

Figures 3 and 4 show grey-scaled 2-D histograms of each (slow-PHA-) channel against another when the detector was illuminated with 300nm photons. Clear correlation can be seen between channels sharing a common STJ (Fig.3). Channels, which do not share a detector, only have a few points off the axes (Fig. 4) which correspond to pile-up events and represent only ~0.08% of the total amount of recorded events in these channels.

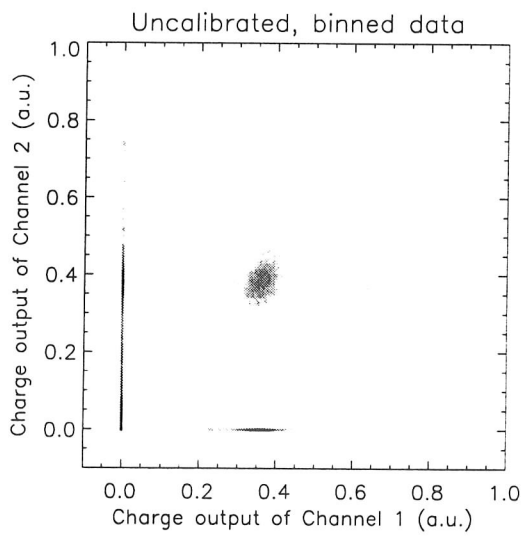

Fig. 3: 2-D Histogram of channel 1 versus channel 2.

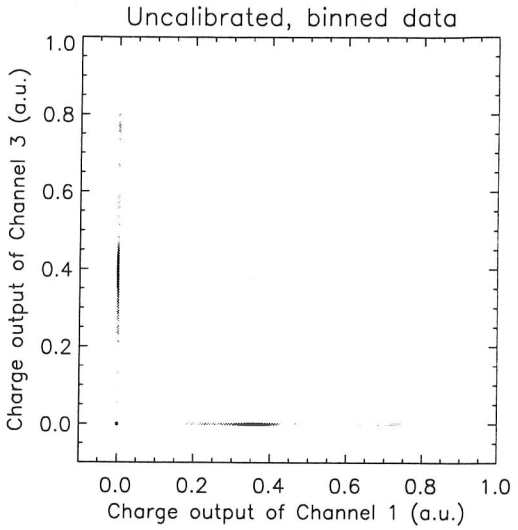

Fig. 4: 2-D Histogram of channel 1 versus channel 3.

3.2 *Spectral Resolution*

For each junction, events were retained by selecting those which had a non-zero signal in both its corresponding channels. For instance for junction J11, valid events were those for which channels 1 and 2 were simultaneously triggered within the coincidence window of 5μs. Average line resolutions obtained were 22, 30 and 78nm (FWHM) at 250, 300 and 500nm respectively, about 11% worse than the traditional individual pixel read-out. When combining the signals from rows and columns, the resolution could be improved to 18, 26 and 62nm, similar to the traditional readout [6].

4 Conclusions

We have presented a novel connection scheme for arrays of pixelated detectors. It drastically reduces the number of wires and circuitry necessary for reading out large array detectors. We have presented results obtained on a 2x2 array of STJs using optical photon excitation. While we have shown that these devices can be properly biased, the energy resolutions obtained are not degraded in this particular case (2x2 array) as compared to the traditional readout scheme.

References

[1] P. Verhoeve, N. Rando, A. Peacock, et al., Proc. of LTD-7, Munich (1997), pp 97-100, ISBN3-00-002266-X.

[2] D.D.E. Martin, A. Peacock, P. Verhoeve, et al., Proc. ISEC 1997, Vol. 3, S40, pp 89-91 (1997).

[3] D.A. Wollman, K.D. Irwin, G.C. Hilton, et al., J. Microsc. 188, 196 (1997).

[4] D.D.E. Martin, A. Peacock, J. Phys. IV France 8, Pr3-225 (1998).

[5] Z.Y. Chang, W.M.C. Sansen, Chapter 5, Kluwer (1991).

[6] D.D.E. Martin, A. Peacock, P. Verhoeve et al., submitted to J. Applied Physics.

The lateral proximity effect and long-range energy-gap gradients in Ta/Al and Nb/Al Josephson junctions

R. den Hartog[1], A. Golubov[2], D. Martin[1], P. Verhoeve[1], A. Poelaert[1], A. Peacock[1], M. Krumrey[3]

[1]*ESA/ESTEC, Astrophysics Division, P.O.Box 299, Space Science Department, 2200 AG Noordwijk, The Netherlands*
[2]*University of Twente, Department of Applied Physics, P.O.Box 217, 7500 AE Enchede, The Netherlands*
[3]*Physikalisch-Technische Bundesanstalt (PTB), Abbestrasse 2-12, 10587 Berlin, Germany*

ESLAB 1999/064/SA

To be published in Proceedings of the 8th International Workshop on Low Temperature Detectors

The lateral proximity effect and long-range energy-gap gradients in Ta/Al and Nb/Al Josephson junctions

Roland den Hartog [a], A. Golubov [b], D. Martin [a], P. Verhoeve [a], A. Poelaert [a], A. Peacock [a], M. Krumrey [c]

[a] *Astrophysics Division, Space Science Dept. of the European Space Agency, ESTEC, P.O. Box 299, 2200 AG Noordwijk, The Netherlands*
[b] *University of Twente, Dept. of Applied Physics, P.O.Box 217, 7500 AE Enschede, The Netherlands*
[c] *Physikalisch-Technische Bundesanstalt (PTB), Abbestr. 2–12, D-10587 Berlin, Germany*

Received 15 August 1999

Abstract

We present two independent experiments, each of which suggests that the local energy gap in Ta (and Nb) has a lateral spatial variation on a scale of several μm. The first experiment is a series of current-voltage characterizations of Nb/Al/AlOx and Ta/Al/AlOx Josephson junctions, which reveals a dependence of the measured energy gap on the size of the junction. This implies a geometrical dependence of the energy gap. An extended version of the current theory of the proximity effect could explain this phenomenon when a lateral coherence length is introduced, which is of the order of the bulk coherence length of the materials.

The second experiment is a series of coincidence measurements of photon absorption events in a Ta absorber between two Ta/Al junctions. There is a clear distinction in the pulse-height characteristics between events detected in the absorber and the junctions. Interestingly, there are also events indicating the presence of a transition region between the absorber and the junction. Event statistics imply that this region has a size of ~6 μm, independent of photon energy, which is quite a bit larger than even the bulk coherence length in Ta. It is argued that an additional effect due to 'smearing' by the relaxed quasi-particle cloud must also be present.

These effects are interesting and intriguing; not only from a theoretical viewpoint, but also for energy-gap engineering of superconducting materials for practical applications, e.g. in a variety of photon and particle detectors.

1 Introduction

When a superconducting material is brought into electrical contact with another (super-)conducting material, the energy gap Δ_{gap} is locally affected. This is in essence the proximity effect. With the advent of modern theoretical descriptions [1, 2, and refs. therein], the proximity effect is now well enough understood to use calculated predictions in the design of superconducting devices. Examples of this 'energy-gap engineering' are given by Poelaert [3]. Up to now most treatments of the proximity effect have been strictly one-dimensional: the variation of the local Δ_{gap} is computed in the same direction as in which the various layers of materials are stacked. However, through a stack of thin films (layer thicknesses of the order of the coherence lengths ξ) the gradient in Δ_{gap} is essentially zero [4]. Quasi-particle (qp) trapping is then the result of differences in the density of states between the layers, resulting in Andreev reflections on the boundary between the materials. In a variety of applications, e.g. photon detectors with absorbers [5–8] or arrays of junctions with high-Δ material bridges [9], the proximity effect may extend over distances in excess of ξ, and the problem will no longer be strictly 1-dimensional. In this paper we discuss two examples of such a situation, which both lead to the conclusion that variations in Δ_{gap} occur over distances of several μm.

2 Current-voltage characteristics of single junctions

2.1 *Measurements*

Fig. 1 summarizes series of measurements on three types of junctions. The Δ_{gap} values are derived from fits to the $\pm 2\Delta$ flanks of the IV curves, which are obtained by scanning the V_{bias} up and down and reading out the current I at a temperature of 0.3 K. Typically, $V_{2\Delta}$ can be determined with an accuracy of a few μV. The first series consists of 11 different samples (with in total 54 junctions) with Nb electrodes (100 – 200 nm thick) and 5 nm Al proximity layers in between. The dependence of Δ_{gap} on the size of the (square) junctions is evident and highly significant. This strongly suggests a spatial variation of the local Δ_{gap} in these junctions. The TEM image clearly shows the undercut in the edge at the location of the Al layer: an unintended by-product of the device patterning process. The second series consist of three samples of in total 28 Ta/Al junctions (100 nm Ta film, with varying Al layer thickness). The TEM image illustrates again how the wet etch has affected the edge. The third set shows three samples of in total 26 Ta/Al junctions

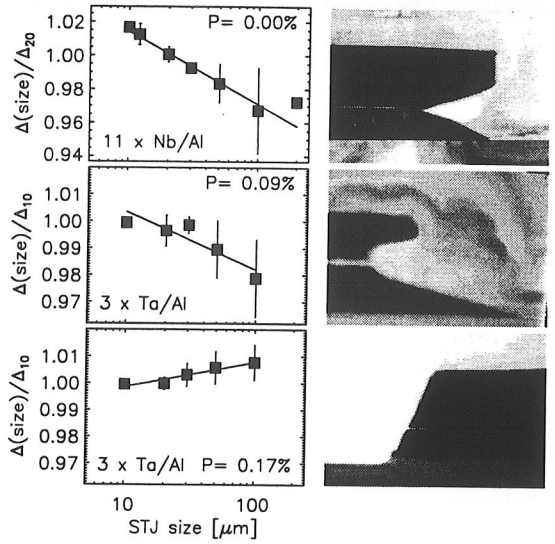

Fig. 1. Left hand column: gap energy Δ_{gap} as a function of junction size. Results for different chips have been combined, hence the normalization of Δ_{gap} for a size that was present in all samples. The probability P for arriving at random at this result is indicated in the inset. Right hand column: TEM cross-section of an edge for a typical junction in the sample. The depth of the undercut is about 200 nm in the two top images.

for which different patterning processes have been tried. This time, the corresponding TEM image shows that the undercut in the edge is absent. At the same time, Δ_{gap} no longer decreases with increasing junction size. Thus we have unambiguous proof of a physical link between the presence of the undercut and the spatial variation of Δ_{gap}. The most obvious explanation for the Δ_{gap} – size relation is that the 0.2 μm wide outer rim which is not in contact with the Al layer due to the undercut, proximizes the electrode in the lateral direction. This rim, which has an elevated gap, surrounds a central region with a lower gap, that corresponds to the normal (vertically proximized) sandwich of Nb (Ta) and Al layers.

2.2 *Modeling*

Starting with the results derived in [1] it is possible to compute the lateral variation in Δ_{gap}. This requires the introduction of an additional, lateral coherence length, $\xi_{||}$, plus a corresponding term in Usadel's equations. The input parameters of these equations, γ_m (associated with the density of states on either side of the Nb/Al or Ta/Al interface), γ_b (associated with the roughness of the interface) and T_C remain unchanged, but an additional boundary condition at the edge is imposed: $\gamma_{m,\,edge} = \gamma_m / 2$ [10]. The results of this 2-dimensional proximity model are shown in Fig. 2 for a range of values of γ_m and γ_b that is compatible with the junctions discussed above. It seems that this model could explain the range of measured Δ_{gap} values in Fig. 1, if we accept two (not so obvious) assumptions: (1) $\xi_{||}$ is of the order of ξ_{bulk} in respectively the Al layer of the Nb/Al junctions and the Ta layer for the Ta/Al junctions.

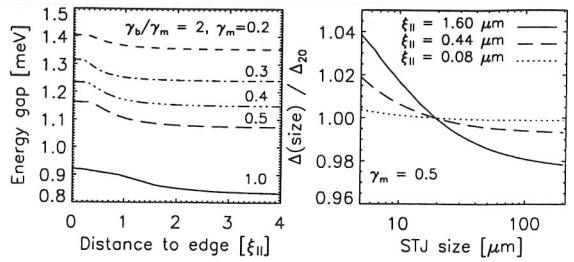

Fig. 2. *a)* The result of theoretical calculations of Δ_{gap} as a function of distance to the undercut edge in units of ξ in the lateral direction, for different values of γ_m. A ratio of $\gamma_b / \gamma_m = 2$ is assumed, consistent with Nb/Al junctions [11]. *b)* The corresponding relations between Δ_{gap} and junction size, for $\xi_{||}$ equal to the bulk ξ of resp. Al, Ta and Nb.

(2) The measured Δ_{gap} is an average over all local gap values, presumably due to imperfections in the superconducting film, in combination with the method of measurement.

We realize that $\xi_{||} \approx \xi_{bulk,\,Al} = 1.6$ μm may be difficult to reconcile with the thickness of the Al layer in the Nb/Al junctions (5 – 10 nm), although the layers below the AlO_x barrier are epitaxial with the monocrystalline sapphire substrate and of high crystallographic quality. In the Ta/Al junctions the effect can not be mediated through the Al layers, since these are polycrystalline on either side of the barrier, with a grain size of ~40 nm. Here, only the Ta base electrode is epitaxial with the substrate, hence $\xi_{||} \approx \xi_{bulk,\,Ta} = 0.4$ μm [12]. An interesting feature of this explanation is that the difference in $\xi_{||}$ would explain the difference in the strength of the effect between the two types of junctions: compare Fig. 1 with Fig. 2b.

3 X-ray absorber experiments

A gradient in Δ_{gap} is also expected (and detected) in the Ta absorber sketched in Fig. 3, at the edges of the junctions. We have probed the effect with a series of coincidence measurements at the PTB SX-700 and FCM beamlines at the BESSY synchrotron rings with photons in the 0.5 – 10 keV energy range. Fig. 4a shows a typical result, which has been transformed in Fig. 4b to coordinates corresponding to event position in the absorber and photon energy,

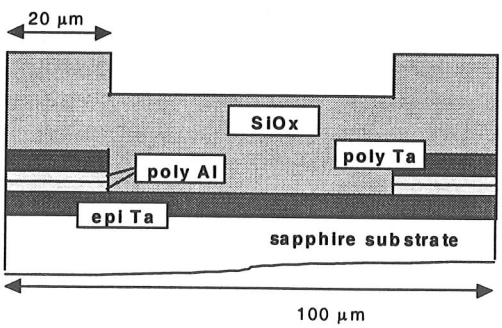

Fig. 3. Sketch of the cross-section of the absorber structure. Layer thicknesses are 480 nm for the SiOx, 100 nm for both the Ta absorber and the Ta counter electrode, and 55 nm for the Al layers. Not indicated is the ~1.5 nm thick AlOx barrier.

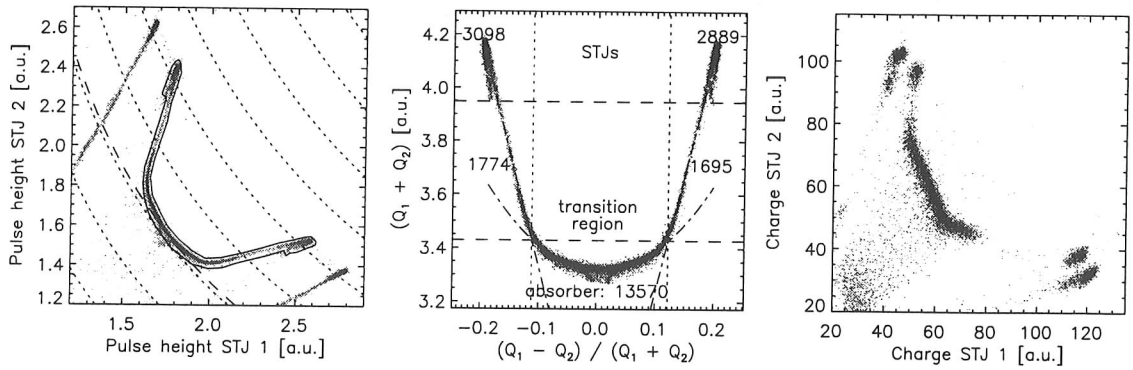

Fig. 4. *a)* Scatter plot of charge signals (in arbitrary units; the STJ response corresponds to ~3 10^7 e^-) detected by junctions on either side of the absorber structure shown in Fig. 3. The dot-dashed curve is a specific fit to the data in the absorber (cf. [8]), short-dashed curves correspond to energies with 0.2 keV spacings. The on-line pulse processing was done using a semi-Gaussian shaping filter with a 4.7 μs time constant. *b)* Transformation to the equivalent of position (horizontal) and total charge (vertical), with event statisitics indicated. The upper horizontal dashed line is based on the expected fraction of events to be detected in the base film underneath the junctions, the lower line is based on the points where both the hyperbolic fit (dot-dashed) to the absorber data and the straight line fits (long dashes) to the data in the transition region between junction and absorber start to diverge significantly from the data. *c)* Same experiment, but now with full pulse sampling using a 40 MHz digital oscilloscope. The charge signal is obtained without filtering through off-line integration of the pulses.

respectively (cf. [8]). It is clear from Fig. 4b that apart from the junctions and the absorber, which have different Δ_{gap} values and therefore different charge responses for the same photon, there is also a transition region. Assuming uniform illumination over the entire structure it is possible to make an estimate of the size of this transition region based on event statistics. We found that over the entire energy range the width of this region is 6 ± 1 μm.

According to Fig. 2a it is unlikely that a gradient in Δ_{gap} is the entire explanation for the presence of the transition region. The absorber consists of epitaxial Ta covered by SiO_x, so the largest $\xi_{||}$ that can reasonably be expected is 0.4 μm

We exclude the possibility that the effect is due to differences in response of the pulse-detection electronics to slow pulses (from the absorber) and fast pulses (from the junctions). Not only would it be unlikely that the onset of the transition would be as sharp as seen in Fig. 4b, but the effect is also present in pulses that were sampled with a digitial oscilloscope without the use of a shaping filter, as can be seen in Fig. 4c.

An alternative explanation is that the Δ_{gap} gradient is 'smeared out' by the qp cloud when it relaxes to its equilibrium energy close to Δ_{gap}. The transition region is then formed by all qp clouds that expand across the step in Δ_{gap}. This would thus imply a radius of 3 μm in epitaxial Ta. A similar number has been suggested for W [13]. As far as we are aware, no detailed calculation has yet been made of the size of the qp cloud after relaxation, but it would be remarkable if it remained equal over a factor of 20 in energy.

Conclusion

In the two experiments that were discussed in this paper we find evidence for gradients in Δ_{gap} on length scales of (at least) several μm. This has some fundamental implications. An analysis of the first experiment, based on the extention of a current proximity model, requires the introduction of a lateral coherence length $\xi_{||}$ that is of the order of the bulk coherence length in the materials at hand. The second experiment implies that the diameter of a relaxed qp cloud could be as large as ~6 μm for photon energies between 0.5 and 10 keV. Although both results raise some questions which remain as yet unanswered, they indicate that lateral Δ_{gap} gradients are likely to play an important role in the performance of thin film superconducting photon detectors.

References

[1] A. Golubov et al., *Phys. Rev.* B 51, 1995, 1073
[2] A.M. Martin, C.J. Lambert, *J. Phys: Cond. Mat.* 8, 1996, L731
[3] A. Poelaert, PhD thesis, UT Twente, 1999, chap. 6
[4] A. Poelaert, PhD thesis, UT Twente, 1999, chap. 2
[5] M.L. van den Berg et al., *Proc. of ASC '98, IEEE Trans. Appl. Supercond.* 9, 1999, 2951
[6] K. Segall et al., *Proc. of LTD-7,* Munich 1997, ISBN 3-00-002266-X, 47
[7] S. Friedrich et al., *Appl. Phys. Lett.* 71, 1997, 3901
[8] H. Kraus et al., *Phys. Lett. B* 231, 1989, 195
[9] P. Verhoeve et al., *Proc. of ASC '98, IEEE Trans. Appl. Supercond.* 9, 1999, 3342
[10] Details of this model will be discussed in a forthcoming publication
[11] A. Poelaert, PhD thesis, UT Twente, 1999, chap. 5
[12] Based on $\xi=\hbar v_F/\pi\Delta_0$ with v_F=1.4 10^6 m/s, cf. K.H. Huang, 1991, Cambridge Univ. PhD thesis.
[13] B. Cabrera et al., *Appl. Phys. Lett.* 73, 1998, 735

We gratefully acknowledge the support of H. Zandbergen of the TU Delft with the production of the TEM images, and stimulating discussions with A. Kozorezov and K. Wigmore of Lancaster University in an earlier stage of this project. All junctions discussed in this paper were produced by the Oxford Instruments Scientific Research Division, Cambridge, UK.

An X-ray Photon-counting Imaging Spectrometer based on a Ta Absorber with four Superconducting Tunnel Junctions

R. den Hartog[1], P. Verhoeve[1], D. Martin[1], N. Rando[1], A. Peacock[1], M. Krumrey[2]
D.J. Goldie[3]

[1]*ESA/ESTEC, Astrophysics Division, P.O.Box 299, Space Science Department, 2200 AG Noordwijk, The Netherlands*
[2]*Physikalisch-Technische Bundesanstalt (PTB), Abbestrasse 2-12, 10587 Berlin, Germany*
[3]*Oxford Instruments, Scientific Research Division, Newton House, Cowley Road, Cambridge Business Park, Cambridge CB4 4WY, United Kingdom*

ESLAB 1999/065/SA

To be published in Proceedings of the 8th International Workshop on Low Temperature Detectors

An X-ray photon-counting imaging spectrometer based on a Ta absorber with four superconducting tunnel junctions

Roland den Hartog[a], P. Verhoeve[a], D. Martin[a], N.Rando[a], A. Peacock[a],
M. Krumrey[b], D.J Goldie[c]

[a]*Astrophysics Division, Space Science Dept. of the European Space Agency, ESTEC, P.O. Box 299, 2200 AG Noordwijk, The Netherlands*
[b]*Physikalisch-Technische Bundesanstalt (PTB), Abbestr. 2–12, D-10587 Berlin, Germany*
[c]*Oxford Instruments Scientific Research Division, Newton House, Cambridge Business Park, Cambridge CB4 4WY, U.K.*

Abstract

We present the first results obtained with a 2-dimensional X-ray imaging spectrometer consisting of a 200x200 μm^2 Ta absorber and read out by four Ta/Al superconducting tunnel junctions (STJs). A preliminary image reconstruction algorithm allows the visualisation of the diffraction pattern from a 5 μm pinhole illuminated with 10 keV X-rays. The image suggests a spatial resolution better than 10 μm. The algorithm does not take into account quasi-particle losses in the absorber. Hence, the pulse height reconstruction is not optimal and the energy resolution varies significantly across the absorber. The best energy resolution is obtained for a 20x20 μm^2 area in the centre of the absorber, and amounts to ~77 eV at a photon energy of 5895 eV, with a 70 eV electronic noise contribution.

1. Introduction

Compared to Si-based CCDs, superconductive detectors such as microcalorimeters and superconducting tunnel junctions (STJs) offer a superior energy resolution, a very broad energy range (from ~1 to >10 keV), and the possibility of single photon counting with high rates (up to several tens of kHz). However, the requirement of individual biasing and read-out of these devices impedes the development of the equivalent of a 1000^2 pixel imaging array [1, 2]. A possible solution is offered by distributed read-out devices (DRODs), in which photons are absorbed in a single crystal of large dimensions [3] or a smaller poly-crystalline layer [4–6], and detected by STJs located at the corners or the edges of the absorber. Compared to an array of STJs, such a detector geometry provides a large sensitive area with a considerable reduction in the number of read-out connections. By time-coincident event measurement it is possible to reconstruct both the absorption position and the energy of the incoming photons. Disadvantages of this approach are the relatively low sustainable count rate and the sensitivity of the absorber to flux trapping.

In this paper we discuss a DROD which combines the advantages of a high-quality epitaxial Ta absorber with a more moderate size of 200 × 200 μm^2, read out by 50 μm square STJs. We present the results of two experiments, which demonstrate the combined spectroscopic and 2-dimensional imaging capabilities of this device. In particular, they imply that weak trapping does not impede good imaging quality. A provisional image reconstruction algorithm is shown to perform remarkably well.

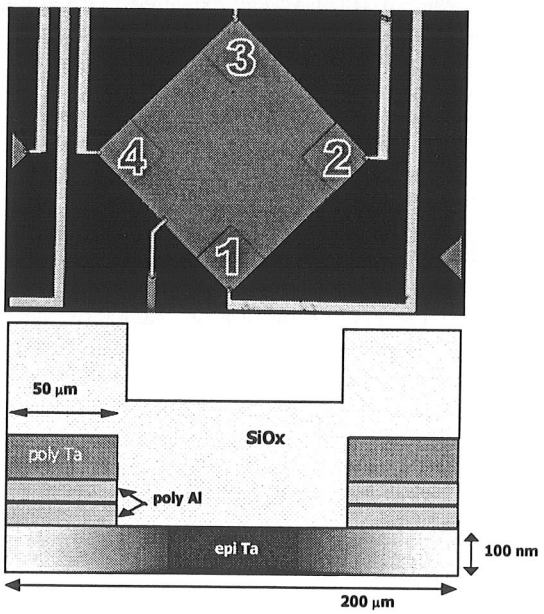

Fig. 1 *a.* A top view image of the tested device, made with a Nomarski microscope. *b.* Sketch of the cross-section. Not indicated are the top-lead connections and the ~1.5 nm thick AlOx between the two Al layers. The SiOx layer is ~480 nm thick, the Al layers are each 55 nm thick. The grayscale gradient in the absorber illustrates the change in energy gap from absorber to junction, due to the proximization of the absorber by the first Al layer in the junctions.

2. Experiments

The detector consists of a 200×200 μm^2 epitaxial Ta absorber with a thickness of 100 nm and a RRR of 48, deposited on a sapphire substrate. Four STJs (50x50 μm^2) are positioned at the corners of the absorber (see Fig. 1a). The STJs are symmetrical, with 100 nm thick Ta layers and 55 nm thick Al trapping

layers. The base Ta is common with the absorber (see Fig. 1b). The device is covered with a 480 nm thick SiOx insulation layer. The STJs have individual Nb connections to their top electrodes and a common Nb return contact via the absorber (see Fig. 1a). The junctions have a normal resistance of 0.1 Ω. The gap energy Δ in the junctions is 0.42 meV.

The first experiment comprised a uniform illumination with a ^{55}Fe source ($E_{K\alpha}$ = 5895 eV and $E_{K\beta}$ = 6490 eV) in our laboratory ^{3}He cryostat (T_{base} = 320 mK). In this well-controlled environment, the IV-curves of the 4 STJs showed subgap currents ~15 nA at a bias voltage of 0.2 mV. From this we derive a quality parameter R_{SG} / R_N = 1.3 10^5. The expected thermal current at 320 mK for these devices is 23 pA. From the shapes of the IV-curves we conclude that the subgap current is due to leakage, and not magnetic flux trapping.

The second experiment was performed at the FCM beamline of the Physikalisch-Technische Bundesanstalt (PTB) at the BESSY II synchrotron facility in Berlin, Germany [7]. The same detector was operated in a portable ^{3}He cryostat (T_{base}=470 mK). In this configuration the IV-curves showed subgap currents of the order of 100 nA. The expected thermal current is 36 nA, plus a leakage current of 15 nA, implies that half of the subgap current was due to magnetic flux trapping. The device was illuminated with 10 keV X-rays through a 5 μm pinhole, located at ~65 cm from the detector. In this configuration the spot size on the detector is completely dominated by the diffraction from the pinhole and the first minimum of the diffraction pattern is expected to be at a radius of ~20 μm from the centre. Note that an energy of 10 keV (close to the end of the energy range of the FCM beamline) is just beyond the Ta L_{III} edge (9881 eV). This ensures a detection efficiency of ~4% in the thin absorber. In both experiments the four STJs were read out simultaneously with charge-sensitive amplifiers with JFET input stages, followed by pulse shaping electronics. For each photon detected as a coincident event in the four STJs, the four pulse heights S_1, S_2, S_3 and S_4 were registered.

3. Image reconstruction

In order to properly convert a set of four charge signals S_1, S_2, S_3 and S_4 to an event position (x, y), we first need a model that predicts (S_1, S_2, S_3, S_4) as a function of (x, y), and then reverse it. At present we are developing a detailed numerical model that takes into account quasi-particle (qp) diffusion, losses and tunneling. For the moment, however, a less thorough, more pragmatic approach was taken in the form of a two-step scheme. First, we compute an intermediate (x^I, y^I):

$$x^I = ½\,\ell\,(-S_1 + S_2 + S_3 - S_4) / (S_1 + S_2 + S_3 + S_4)$$
$$y^I = ½\,\ell\,(-S_1 - S_2 + S_3 + S_4) / (S_1 + S_2 + S_3 + S_4),$$

where ℓ is the size of the absorber (200 μm). Next, we refine these coordinates using a simple model that takes into account the solid angle subtended by each junction at a given photon-absorption position. No corrections are made at this stage for qp losses in the absorber. Such losses give rise to a reduction of the measured pulse height, depending on the distance of the absorption position to the STJ and distortions of the image. This will affect the image quality as well as the energy resolution.

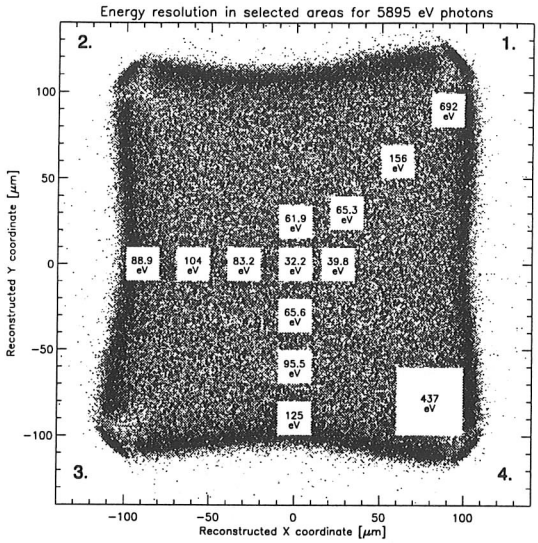

Fig. 2. The intrinsic energy resolution ΔE (FWHM) for 6 keV photons, as a function of position. The ~70 eV electronic noise contribution has been subtracted. The white areas indicate the events that were selected for the computation of the local ΔE. The signals have not been corrected for qp losses prior to the computation of ΔE. The position of each event was derived from the combined signals of the 4 STJs in a two step scheme. A slight asymmetry is visible on the left side, due to the presence of the base contact lead.

4. Results

Figure 2 shows the image obtained by uniform illumination with photons from a Fe^{55} source. Only absorber events corresponding to Mn-K_α (5895 eV) or Mn-K_β (6490 eV) are shown. The higher density of events near the edges is an artifact from our image reconstruction algorithm. Apart from this, it yields a reasonably square image, with only slight distortions at the edges and a uniform distribution of events, even in the corners. This is remarkable, given the relatively large sizes of the junctions. The apparent success of this simple algorithm is largely due to the fact that we are in a weak-trapping regime. For the events in the box in the upper right-hand corner, STJ 3 detects still 60% of the signal that STJ 1 detects, even though it is at a maximum distance away from the absorption sites. Moreover, the 'blobs' in the four corners of Fig. 2, which are associated with events absorbed directly underneath the STJs, contain only 2% of the total number of events, instead of 25%, as one would expect from the geometry of the device. The low-density regions in the corners indicate where these 2%

trapped events originate. For the remaining 98% of the events, whether or not absorbed underneath an STJ, it is possible to determine a position.

The white boxes in Fig. 2 are selected regions for which the energy resolution was determined. The numbers quoted in the boxes are obtained after the subtraction of a 70 eV electronic noise contribution. It is clear that the energy resolution is far from uniform across the absorber. In comparison, the total detected charge is much more uniform, implying that qp losses cannot fully explain the degradation of ΔE away from the center. Side events give ~1.5% more charge than center events, and corner events ~4% more charge than center events. Hence the average charge gradient across a 20 × 20 μm^2 box due to qp losses is maximally 0.8%, equivalent to 48 eV. This is not sufficient to explain even the observed degradation near the centre. However, in reality a part of the events were absorbed outside the box, but were included as a result of uncertainties in the position reconstruction. A positional uncertainty Δx of ~10 μm will roughly double the effective box area, which would suffice to explain the ΔE degradation near the center. The poor ΔE in the corners might also be the partly the result of a strong spatial gradient in the local energy gap, caused by the proximity effect from the first Al layer in the STJs [8]. This gradient is presumably 'smeared' in the lateral direction by the finite size of the relaxed qp cloud. Once we have a more accurate model of the signal responses of the STJs as a function of event absorption position in the absorber, it should be possible to correct for the losses and derive a more uniform ΔE. This has already been demonstrated for 1-dimensional DRODs [9].

Figure 3 shows an image obtained with 10 keV illumination through a 5 μm pinhole. In this case the image reconstruction gives a less satisfactory result than in Fig. 2. This is most likely due to magnetic flux trapping in the absorber, which causes localized enhancements of the qp losses, and for which we already discussed evidence in the IV curves in section 2. Nevertheless, the first minimum and second maximum of the Fraunhofer diffraction (separated by 6 μm) pattern are clearly visible. So we judge from Figs. 2 and 3 that $\Delta x \approx 5 - 10$ μm. In the case of perfect trapping at the STJs one has $\Delta x / \ell \approx \Delta E / E$, where ℓ is the absorber size [4]. A resolution $\Delta E / E \approx 1\%$, as we measure in the central parts of the absorber, would then imply a spatial resolution Δx of 2 μm. Despite the fact that we are in a weak-trapping regime and the relation between spatial and energy resolution is probably no longer true, it appears that we are still not too far away from this prediction.

Conclusions

We have presented the first results obtained with a 2-dimensional DROD used as an X-ray photon-counting imaging spectrometer, based on a high-quality Ta absorber read out by four STJs. These results illustrate the potential of this design: imaging capability over a large effective area, with a high spatial resolution, and a small number of electrical connections. They also indicate that there is still room for improvement, in particular in the energy resolution. Although our simple, provisional image reconstruction algorithm performs remarkably well, it needs eventually to be replaced by a more physically motivated procedure that includes qp losses and diffusion.

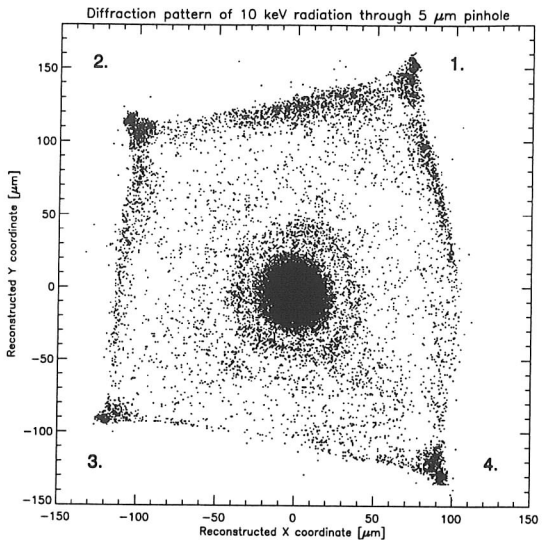

Fig. 3. A Fraunhofer diffraction pattern created with 10 keV photons through a 5 μm pinhole at the KMC beamline of the Bessy II synchrotron facility [8]. The distance between the first minimum and the second maximum is 6 μm. The fact that we can clearly see both indicates that the spatial resolution Δx cannot be much worse than that. Although we are using the same image-reconstruction algorithm as in Fig. 2, the resulting image is more distorted. This is most likely due to magnetic flux trapping in the absorber, as the magnetic environment of this experiment was less optimal

References

[1] D. Martin et al., these proceedings
[2] P. Verhoeve et al., *Proc. of ASC '98, IEEE Trans. Appl. Supercond.* 9, 1999, 3342
[3] M.L. van den Berg et al., *Proc. of ASC '98, IEEE Trans. Appl. Supercond.* 9, 1999, 2951
[4] H. Kraus et al., *Phys. Lett. B* 231, 1989, 195
[5] K. Segall et al., *Proc. of LTD-7,* Munich 1997, ISBN 3-00-002266-X, 47
[6] S. Friedrich et al., *Appl. Phys. Lett.* 71, 1997, 3901
[7] B. Beckhoff et al., these proceedings
[8] R. den Hartog et al., these proceedings
[9] P. Verhoeve et al., these proceedings

We gratefully acknowledge the assistance of J. van der Biezen from ESTEC with the production of the Nomarski image, and the support of the PTB crew at Bessy II, in particular outside regular working hours. The device discussed in this paper was produced by the Oxford Instruments Scientific Research Division, Cambridge, UK. Finally, we would like to thank the referee for several useful comments that improved the presentation of this paper.

Quasiparticle Energy Relaxation in Superconducting Tunnel Junction used as Photon Detectors

A. Poelaert[1], A. Golubov[2], A. Peacock[1], R. den Hartog[1], H. Rogalla[2]

[1]*ESA/ESTEC, Astrophysics Division, P.O.Box 299, Space Science Department, 2200 AG Noordwijk, The Netherlands*
[2]*University of Twente, Department of Applied Physics, P.O,Box 217, 7500 AE Enchede, The Netherlands*

ESLAB 1999/066/SA

To be published in Proceedings of the 8th International Workshop on Low Temperature Detectors
Dalfsen – The Netherlands, 15-20 August 1999

QUASIPARTICLE ENERGY RELAXATION IN SUPERCONDUCTING TUNNEL JUNCTION USED AS PHOTON DETECTORS

A. Poelaert[1], A. Golubov[2], A. Peacock[1], R. den Hartog[1], H. Rogalla[2]

[1]Astrophysics Division of the European Space Agency, Noordwijk, The Netherlands.
[2]Low Temperature Group of the Faculty of Applied Physics, University of Twente, The Netherlands.

Abstract

We exploit the results of recent work [1] showing that energetic quasiparticles in a superconductor relax to an energy, called *balance energy*, larger than the superconducting energy gap, despite of the large density of states available at the gap. This feature has a major impact on the performance of superconducting tunnel junctions used as photon detectors. We show how the balance energy and the parameters for photon detection are sensitive to the superconducting proximity effect. In particular, we show that the balance energy also exists for non proximized structures, obeying the BCS theory.

1. INTRODUCTION

The energy of a photon absorbed in an electrode of a superconducting tunnel junction (STJ) is converted into a number of quasiparticles (QPs) proportional to the photon energy. QPs result from Cooper pair (CP) breaking in one of the superconducting electrodes of the STJ. They are excited states governing the physics of free electrons in a superconductor (i.e. electrons not bound in a CP), and are therefore associated with charge carriers.

Recent theoretical and experimental evidence indicates that initial energetic QPs do not relax down to the superconducting energy gap. During the photon detection process, QPs stay at a higher energy, called *balance energy*. The balance energy arises from a trade-off between processes that decrease QP energy decrease (relaxation with phonon emission) and those increasing QP energy (phonon absorption and tunneling). In order to estimate the balance energy, it is important to establish the various characteristic times involved in the photon detection process as a function of QP energy. In this paper, we use the results of [1] to show (1) how the characteristic times are sensitive to the superconducting proximity effect in multi-layered electrodes and (2) that a balance energy larger than the energy gap is present in any structure, proximized or not. We start the discussions from an existing Ta/Al proximized device.

2. DEVICE CHARACTERISTICS

The device is a 20×20 μm^2 Ta/Al STJ deposited on highly polished sapphire. 100 nm of epitaxial Ta were first deposited onto the sapphire, followed by 55 nm of Al. A 1.5 nm thick AlO_x barrier with a resistivity ~ 4.2 $\mu\Omega$ cm^2 follows. The polycrystalline top electrode is deposited onto the barrier. It consists of 55 nm of Al and 100 nm of Ta, separated by 4 nm of Nb. A gap $\Delta_g = 450$ μeV was measured.

3. PROXIMITY EFFECT PARAMETERS

The superconducting proximity effect is the effect of the mutual interaction between two or more superconducting layers in electrical contact. The model used to determine the properties of proximized structures is fully described in [2]. For each sub-layer S_i in the proximized structure, the so-called Usadel equations can be solved, with the proper boundary conditions at the layer interfaces. These equations provide the CP potential $\Delta_{S_i}(x)$ and a complex Green function $\vartheta_{S_i}(\omega_n, x)$ representing the density of states. Here, $\omega_n = \pi T(2n+1)$, $[n = 1,2,\ldots]$ are the Matsubara frequencies, related to the continuum states energy ε by $\varepsilon = -i\omega_n$, and x is the position normal to the plane interfaces between successive layers ($x = 0$ at the barrier in this paper).

The boundary conditions for a bilayer $S_1 - S_2$ are generally expressed in terms of the proximity effect parameters γ and γ_B defined as $\gamma = \rho_{S_1}\xi^*_{S_1} / \rho_{S_2}\xi^*_{S_2}$ and $\gamma = R_B / \rho_{S_2}\xi^*_{S_2}$. Here R_B is the resistance of the $S_1 - S_2$ interface multiplied by its surface, and ρ_{S_i} is the normal state resistivity of layer S_i. The normalized coherence lengths $\xi^*_{S_i}$ are given by $\xi^*_{S_i} = \xi_{S_i}\sqrt{T_{c,S_i} / T_{c,S_1}}$, where ξ_{S_i} and T_{c,S_i} are the coherence length and critical temperature in S_i. γ_B represents the transparency of the $S_1 - S_2$ interface, whereas γ quantifies the respective impact of S_1 and S_2 on the entire bilayer.

Estimating γ and γ_B provides the density of states in a given proximized electrode. These parameters can be determined by comparing experimental and theoretical values for the critical current J_c and for

the gap Δ_g. The experimental values can be found as a function of temperature from the IV characteristics of the device. The theoretical gap can be extracted directly from the calculated density of states. The critical current can be calculated with the help of the following equation:

$$\frac{eJ_c R_N}{2\pi T_c} = \frac{T}{T_c} \sum_{\omega_n>0} \left[\sin \vartheta_{S_2}\left(\omega_n, x=-d_{S_2}\right)\right]^2 . \quad (1)$$

Here, R_N is the barrier resistance. The density of states has been taken identical in both electrodes.

The results of such a fit for the device described in Section 2 is shown in Fig. 1. The best match has been found for $\gamma = 0.05$ and $\gamma_B = 3$. Typical examples of deviations of γ and γ_B are also shown (solid lines for γ and dashed lines for γ_B).

4. CHARACTERISTIC TIMES

The characteristic times of processes affecting the QP energy (and thereby determining the balance energy) are the tunnel time τ_{tun}, the relaxation time τ_e and the phonon absorption time τ_a. The expression for these quantities can be found in [1]. Numerical calculations, corresponding to the theoretical curves of Fig. 1, are shown in Figs. 2 (τ_{tun}), 3 (τ_e) and 4 (τ_a). All quantities are calculated for the whole proximized structure. Any position dependence within a structure is removed by averaging over the density of states.

Noting that in Ta most of the states are above Δ_{Ta}, clear statements can be made from Figs 2 to 4. Firstly, a transparent interface (small γ_B) favours these high-energy states in Ta, and promotes tunneling and phonon absorption. Phonon emission is degraded at small γ_B due to the large value of Δ_g. On the other hand, favouring Ta to the expenses of Al (large γ) favours tunneling, phonon emission and absorption for QPs above Δ_{Ta}, while these same processes are degraded below Δ_{Ta}. Clearly, the deposition process of successive superconducting layers can have a major impact on the process of QP relaxation, with subsequent consequences on the STJ performance, including charge output and energy resolution.

5. BALANCE ENERGY

The balance energy E_b is defined as the energy at which the processes enhancing the QP energy (excitation) exactly compensate for relaxation. In a STJ, relaxation is performed via phonon emission only, while excitation occurs via phonon absorption or tunneling. In other words, the balance energy $E_{b,\mathrm{STJ}}$ in a STJ is such that

$$\left[\tau_{tun}\left(E_{b,\mathrm{STJ}}\right)\right]^{-1} + \left[\tau_a\left(E_{b,\mathrm{STJ}}\right)\right]^{-1} = \left[\tau_e\left(E_{b,\mathrm{STJ}}\right)\right]^{-1} . \quad (2)$$

In a system where tunneling is absent, such as a superconducting absorber, we simply have

$$\tau_a\left(E_{b,\mathrm{absorber}}\right) = \tau_e\left(E_{b,\mathrm{absorber}}\right) . \quad (3)$$

In this paragraph we want to discuss the consequences of the proximity effect on the balance energy. Starting from the device described in sections 2 and 3, the proximity effect is 'tuned' by changing the Al thickness only. The thickness and properties of the Ta layer and the resistance of the Al/Ta interface remain unchanged. In terms of the proximity effect parameters, it means that $\gamma/\gamma_B = \rho_{Ta}\xi_{Ta} / R_b$ is a constant and $\gamma \propto \sqrt{d_{Al}}$ for clean superconductors [1]. It must be stressed however that in practice, only the base electrode is in the clean limit and that the relation $\gamma \propto \sqrt{d_{Al}}$ is not entirely true. However, this does not seem to affect the conclusions of this work.

The balance energy (relative to the gap Δ_g) is plotted as a function of d_{Al} in Fig. 5. Line 1 corresponds to Eq. (2) and line 3 to Eq. (3). The dashed line corresponds to Eq. (2) where phonon absorption has been neglected. It appears that in a tunneling system, absorption is very slow, and excitation is mainly governed by tunneling. On the other hand, in the absence of tunneling, phonon absorption also inhibits QP relaxation to the gap. At a thickness of 2 nm of Al, the electrode can be viewed as an almost pure Ta layer, close to the BCS limit. Even in this case, QP relaxation to the gap cannot be achieved. In all cases, the balance energy is at least 5% above the gap. In a system with tunneling, it is 15% to 50% above the gap.

Fig. 5 shows that QP relaxation is more difficult in proximized structures than in BCS-like structures. The main consequence of this fact is that, in a proximized structure, QPs will be more widely distributed around the balance energy. This has direct implications on the intrinsic energy resolution of the device, due to statistical fluctuations of the energy-dependent parameters involved in the photon detection process.

6. CONCLUSIONS

We have described a method to calculate the characteristic times for QPs involved in the photon detection process in a STJ, taking into account the superconducting proximity effect. A major outcome from this work is that QP relaxation does not occur down to the energy gap. A balance between relaxation processes (phonon emission) and

excitation processes (phonon absorption and tunneling) is observed, and maintains the QPs at the balance energy. We have shown that the balance energy is significantly above the gap, even when tunneling does not take place, and even in a BCS, non-proximized structure. In future work, attention will be paid on the implications of the balance energy on the performance of STJs used as photon detectors, especially in terms of energy resolution.

7. REFERENCES

1. A. Poelaert, Ph.D. thesis, University of Twente (1999).
2. A. Poelaert et al., presented at the 2nd Conference on New Developments in Photodetection, Beaune, June 1999.
3. A. Golubov et al., Phys. Rev. B **51**, 1073 (1995).

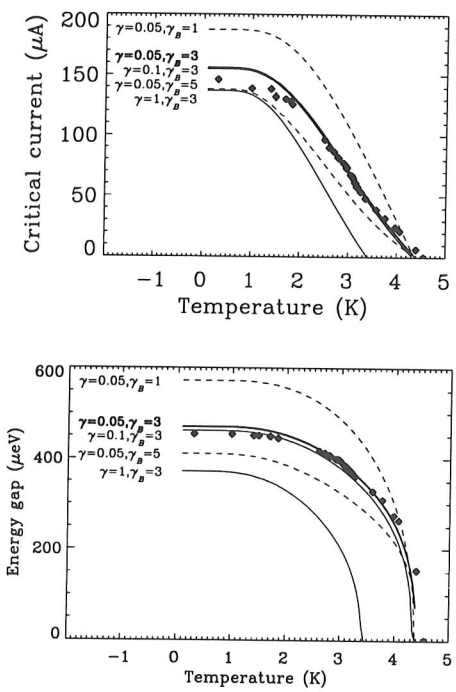

Figure 1. Critical current (top) and energy gap (bottom) as a function of temperature: experimental data (diamonds) and theoretical curves.

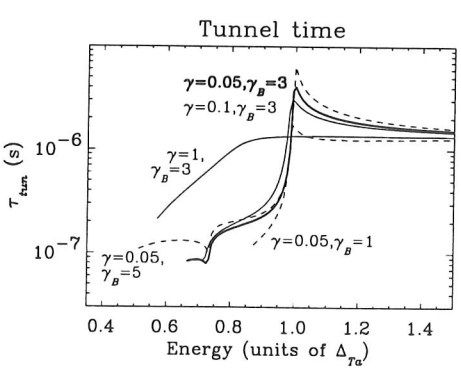

Figure 2. Tunnel time as a function of QP energy for different values of γ and γ_B.

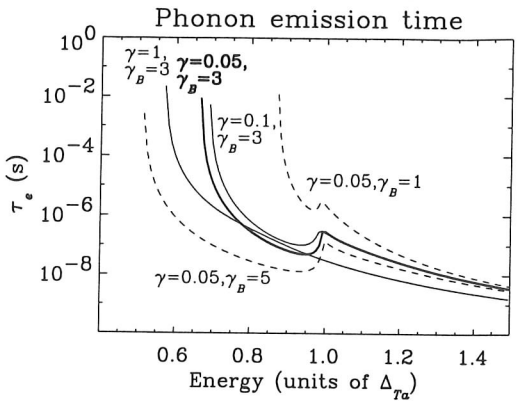

Figure 3. Phonon emission time as a function of QP energy for different values of γ and γ_B.

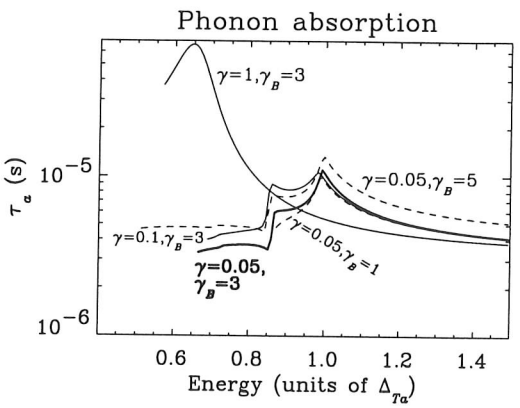

Figure 4. Phonon absorption time as a function of QP energy for different values of γ and γ_B.

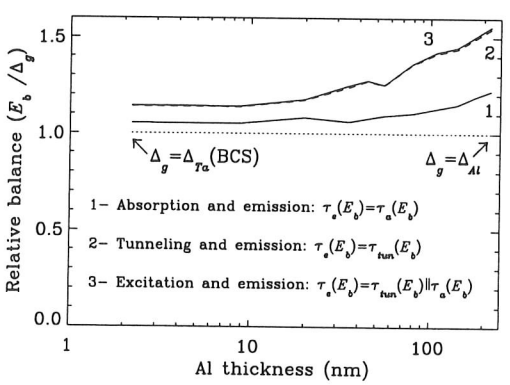

Figure 5. Balance energy as a function of Al thickness for Ta/Al electrodes, with 100 nm of Ta and proximity effect parameters consistent with the real device measured in Fig. 1.